Washington University in St. Louis
Washington University Open Scholarship

All Theses and Dissertations (ETDs)

January 2010

Statistical Design And Imaging Of Position-Encoded 3D Microarrays

Pinaki Sarder
Washington University in St. Louis

Follow this and additional works at: https://openscholarship.wustl.edu/etd

WASHINGTON UNIVERSITY IN ST. LOUIS

School of Engineering and Applied Science

Department of Electrical & Systems Engineering

Dissertation Examination Committee:
Prof. Arye Nehorai, Chair
Prof. Hiro Mukai
Prof. Jr-Shin Li
Prof. Dibyen Majumdar
Prof. R. Martin Arthur
Prof. Samuel Achilefu

STATISTICAL DESIGN AND IMAGING OF POSITION-ENCODED 3D

MICROARRAYS

by

Pinaki Sarder

A dissertation presented to the Graduate School of Arts and Sciences
of Washington University in partial fulfillment of the
requirements for the degree of

DOCTOR OF PHILOSOPHY

May 2010
Saint Louis, Missouri

ABSTRACT OF THE DISSERTATION

Statistical Design and Imaging of Position-Encoded 3D Microarrays

by

Pinaki Sarder

Doctor of Philosophy in Electrical Engineering

Washington University in St. Louis, May 2010

Research Advisor: Professor Arye Nehorai

We propose a three-dimensional microarray device with microspheres having controllable positions for error-free target identification. Here targets (such as mRNAs, proteins, antibodies, and cells) are captured by the microspheres on one side, and are tagged by nanospheres embedded with quantum-dots (QDs) on the other. We use the lights emitted by these QDs to quantify the target concentrations. The imaging is performed using a fluorescence microscope and a sensor.

We conduct a statistical design analysis to select the optimal distance between the microspheres as well as the optimal temperature. Our design simplifies the imaging and ensures a desired statistical performance for a given sensor cost. Specifically, we compute the posterior Cramér-Rao bound on the errors in estimating the unknown target concentrations. We use this performance bound to compute the optimal design variables. We discuss both uniform and sparse concentration levels of targets. The uniform distributions correspond to cases where the target concentration is high or the time period of the sensing is sufficiently long. The sparse distributions correspond to

low target concentrations or short sensing durations. We illustrate our design concept using numerical examples.

We replace the photon-conversion factor of the image sensor and its background noise variance with their maximum likelihood (ML) estimates. We estimate these parameters using images of multiple target-free microspheres embedded with QDs and placed randomly on a substrate. We obtain the photon-conversion factor using a method-of-moments estimation, where we replace the QD light-intensity levels and locations of the imaged microspheres with their ML estimates.

The proposed microarray has high sensitivity, efficient packing, and guaranteed imaging performance. It simplifies the imaging analysis significantly by identifying targets based on the known positions of the microspheres.

Potential applications include molecular recognition, specificity of targeting molecules, protein-protein dimerization, high throughput screening assays for enzyme inhibitors, drug discovery, and gene sequencing.

Acknowledgments

Dedicated to my parents.

Contents

List of Tables

List of Figures

Chapter 1

Introduction

Microarray devices are used to measure concentrations of targets such as mRNAs, proteins, antibodies, and cells [1]. Conventional microarrays are two-dimensional (2D) [2]; they employ circular spots positioned in predefined locations and conjugated in surface with molecular probes to capture targets. Thus, they have position encoding which avoids target identification errors.

Recently, a 3D microarray technology has been developed [1], [3], [4]. The main advantages of 3D microarrays over 2D are their directional binding capability, higher sensitivity, and higher surface-to-volume ratio that offers faster reaction. The microspheres in 3D microarrays are conjugated in surface with molecular probes to capture targets, and contain quantum-dot (QD) barcodes to identify the captured targets. Optical reporters (e.g., fluorescent dyes, QDs, nanospheres) are employed to quantify the target concentrations [5], [6]. Their imaging is performed using a fluorescence microscope and an image sensor.

In existing 3D microarrays, the microspheres are typically randomly placed on a substrate [1], [3], [4]. Such random placement of the microspheres renders their packing inefficient. It also hampers the quality of the imaging in areas where the microspheres

are closely clustered, and it makes the automatic imaging analysis difficult. Additionally, the existing 3D microarrays are prone to errors in identifying targets, due to noise in the measured QD barcode spectra.

To overcome these drawbacks, we propose a new (compact) 3D microarray layout with determinate microsphere positions. These microspheres are thus position encoded, similar to the spots in the 2D microarrays, thus identifying targets without errors through position encoding and simplifying significantly the data processing. We surround the microspheres (captured with targets) with nanospheres embedded with QDs. We use these QD lights to quantify the target concentrations. We develop a statistical design approach to select the minimal distance between the microspheres for a desired performance in imaging the proposed microarray and achieve an efficient microsphere packing. We also compute the optimal operating temperature of the image sensor fitting this performance, considering that the cost of such sensors varies proportionally with their cooling requirements. Thus, our proposed design ensures a desired statistical imaging performance for a given image sensor cost. The feasibility of implementing the proposed 3D microarray layout with the position-encoded microspheres is being demonstrated in a parallel research effort by our collaborators.

Some of the key advantages of the proposed microarray over existing 3D microarrays are efficient packing, high sensitivity, simplified imaging, and guaranteed accuracy in estimating the target concentrations, as we discuss in more detail in Sections 2.1 and 2.3.

We estimate the intensity levels and locations of multiple target-free and QD-embedded microspheres from their images. We use these estimates to compute the photon-conversion factor of the image sensor that we replace in the design. We thus image

multiple QD-embedded microspheres, and develop a method to obtain their intensity level and location estimates. We exploit here the prior information of the light-intensity profiles of the microspheres, and thus achieve a better accuracy than the existing blind-deconvolution algorithms [7], [8]. Our method enables high performance for any next-stage image analysis with the proposed microarray.

The dissertation is organized as follows. In Chapter 2, we present our work on statistical design of position-encoded 3D microarrays. In Chapter 3, we discuss our work on estimating intensity levels of QD-embedded microspheres. We summarize our contributions in Chapter 4 and also propose future work.

Chapter 2

Statistical Design of Position-Encoded 3D Microarrays

In this chapter, we present our statistical design of position-encoded 3D microarrays. Namely, we first construct a statistical measurement model, assuming the imaging is space-variant and employing the classical three-dimensional (3D) point-spread function (PSF) proposed in [9]. We consider that the target distributions on the microspheres are either uniform or sparse. The uniform distributions correspond to cases where the target concentration is high, or the time period of the sensing is sufficiently long. The sparse distributions correspond to low target concentrations or short sensing durations. We assume the target concentrations are unknown, with known prior distributions, and the noise is additive Gaussian. We optimize the design by computing the sum of the posterior Cramér-Rao bounds (PCRBs) [10] on the errors in estimating the target concentrations. In computing this performance measure, we substitute the maximum likelihood (ML) estimates for the photon-conversion factor of the image sensor and its background noise variance. We use the resulting estimated performance measure to compute the optimal distance and temperature.

The chapter is organized as follows. In Section 2.1, we describe the configuration and imaging of the proposed microarray. In Section 2.2, we compute the PCRB on the errors in estimating the target concentrations in imaging the proposed device. In Section 2.3, we present our method to compute the optimal distance and temperature. In Section 2.4, we present our estimation method. In Section 2.5, we show our results obtained in the numerical examples.

2.1 Position-Encoded Microarray Device

We discuss the configuration of the proposed microarray, its image-acquisition procedure, and its image analysis advantages compared to the existing 3D microarrays.

2.1.1 Sensing Device Configuration

Figure 2.1(a) illustrates a schematic diagram of our proposed position-encoded compact 3D microarray device. We assume that all the microsphere centers are positioned in a plane parallel to the xy plane. Here we place the microspheres in a uniform 2D grid in controllable positions. For simplicity, we represent them without their dedicated receptors. The microspheres are made of polystyrene and are around $5\mu m$ in diameter. For each microsphere, we encode specific receptors (antibody molecules) to detect a target of interest. Thus, we identify each target without errors from each microsphere location. We term this property as position encoding for 3D microarrays. By coding different microspheres with corresponding receptors, we are able to identify multiple targets simultaneously without errors.

To optimally design the layout of the proposed device, we compute the minimal distance d_{opt} between the microspheres to estimate the target concentrations with a desired accuracy. This optimal design maximizes the microsphere packing in the proposed microarray.
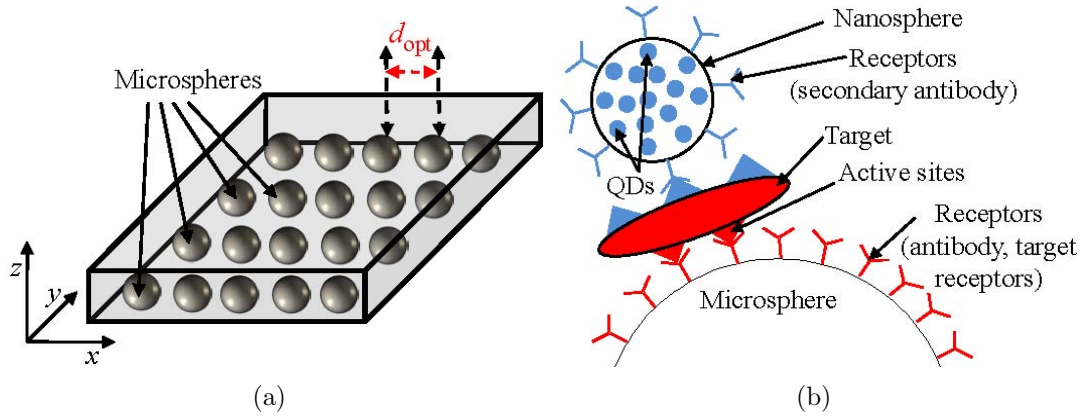
Figure 2.1: (a) Schematic of a position-encoded three-dimensional microarray, where the microspheres are separated by an optimal distance. (b) A target molecule captured on a microsphere.

To detect and quantify the targets, we use nanospheres ($\sim$ 100nm in diameter) embedded with identical quantum-dots (QDs) and conjugated with receptors. The nanospheres allow label-free targeting (targets do not contain any optical reporter, and thus their structures and chemical properties remain unchanged), on-off signaling, and enhance the detection sensitivity [1]. The targets are captured by the microspheres on one side, and are tagged by the nanospheres on their other side, see Figure 2.1(b).

Thus, the main differences (mentioned so far) between the configurations of the proposed and existing 3D microarrays are the proposed position encoding and optimal selection of the minimal distance between the microspheres to estimate the target

concentrations with a desired accuracy. Also, the position encoding offers higher sensitivity. Namely, in existing 3D microarrays two or more microspheres often come in close proximity of each other, and hence the receptors in that close-proximity region are unable to capture targets. This reduces the sensitivity of the existing 3D microarrays. In contrast, the microspheres in our proposed microarray do not come close to each other as their microsphere positions are controllable, and hence the sensitivity of our proposed microarrays is higher.

2.1.2   Preparing and Collecting Data

To physically prepare the data, we propose to follow the procedure for the 3D microarray in [1], except for identifying the targets. Namely, a microfluid stream with the targets is passed through the sensors, and then a cocktail of nanospheres is released periodically [1]. The targets bind to the intended microsphere surfaces on one side and to the nanospheres on the other side (Figure 2.1(b), showing one target and one nanosphere as an example) [1]. All nanosphere QDs emit light upon excitation by UV light, and produce a source of light in the form of a spherical shell around each microsphere. The levels of the shell lights quantify the target concentrations. We identify the targets using the known positions of the microspheres. This is in contrast to other approaches [1], where the targets are identified by the colors of QD barcodes in the microspheres, creating possible errors.

To collect the data, we propose to follow again the procedure in [1]. Namely, to image the target-captured specimen, a fluorescence microscope is focused at different depth planes of the ensemble, parallel to the xy plane of the target-free device shown in Figure 2.1(a); see also Figure 3.1 in Chapter 3. This produces a series of 2D

cross-section images of lights emitted by the nanosphere QDs, see [11]. Thus, each cross-section image of the spherical shell light formed around a microsphere forms the image of a ring.

To capture the images, a CCD or CMOS image sensor with high quantum efficiency [12], i.e., with high sensitivity, is employed. Examples of such sensors are those produced by Watec Inc. or Micron Inc. [13], [14]. Sensors produced by these companies have high sensitivity, but require temperature cooling using external electronics to reduce the background noise. The cost of such sensors proportionally varies with their cooling requirements. Thus, we propose to select the optimal operating temperature of the image sensor as a trade-off between minimal cooling vs. maximal estimation accuracy, using our statistical performance results as a function of the distance between the microspheres and temperature in their image sensing.

2.1.3 Image Analysis Comparison with Existing 3D Microarrays

Analyzing the images of the proposed microarrays should be significantly simpler and more accurate than in existing 3D microarrays, where the random microsphere placement often causes some imaged microspheres to cluster [4], [15]. Also, the number of the segments in these imaged microspheres in existing 3D microarrays is not known *a priori*. Furthermore, their QD barcode spectra for the target identification are noisy [4]. Imaging such randomly placed microspheres requires complex segmentation and estimation of their number. Identification of targets from the noisy QD light barcodes in the existing 3D microarrays requires computations and is prone to errors.

In contrast, our proposed microarrays do not require such computations for segmentation or target identification, and has no such errors. This is useful, for example, for simultaneous imaging of multiple targets.

2.2 Performance Analysis

We present a statistical performance analysis for estimating the target concentrations from our proposed device. We first describe the measurement model for the fluorescence microscopy imaging of the proposed device with targets captured on microspheres and with nanosphere QD lights. We then derive the performance bounds on the errors in estimating the target concentrations, for the statistical design.

2.2.1 Measurement Model

The measurement at the image sensor output, in fluorescence microscopy imaging of a QD illuminating object, is (see [15])

$$g(x, y, z; \boldsymbol{\theta}) = \tilde{s}(x, y, z; \boldsymbol{\theta}) + w_{\mathrm{P}}(x, y, z; \boldsymbol{\theta}) + w_{\mathrm{b}}(x, y, z), \qquad (2.1)$$

where $x \in \{x_1, x_2, \ldots, x_K\}$, $y \in \{y_1, y_2, \ldots, y_L\}$, and $z \in \{z_1, z_2, \ldots, z_M\}$; K, L, and M denote the numbers of measurement voxels; $\boldsymbol{\theta}$ is the unknown random parameter vector in imaging; $\tilde{s}(x, y, z; \boldsymbol{\theta})$ is the microscope output; $w_{\mathrm{P}}(x, y, z; \boldsymbol{\theta})$ is a zero-mean Gaussian noise with variance $\tilde{s}(\cdot)/\beta$, and β is the photon-conversion factor of the image sensor [16], [17]; $w_{\mathrm{P}}(\cdot)$ models the interference due to the photon counting process in the image sensor, and is independent from voxel to voxel; $w_{\mathrm{b}}(x, y, z)$ models

the background noise which is a zero-mean Gaussian noise with variance σ_{b}^2 [15]; $w_{\mathrm{b}}(\cdot)$ is due to the thermal noise[1] of the image sensor [18], is independently and identically distributed (iid) from voxel to voxel, and is statistically independent with $w_{\mathrm{P}}(\cdot)$. Thus, $g(x, y, z; \boldsymbol{\theta})$ is Gaussian distributed with mean $\tilde{s}(\cdot)$ and variance $\tilde{s}(\cdot)/\beta + \sigma_{\mathrm{b}}^2$, independent from voxel to voxel [15]. In this chapter, we assume that the image sensor output is free of constant offset [18]. We also assume β and σ_{b}^2 are known. Otherwise, we estimate them using images captured from a training experiment, see Section 2.4.

Assuming a space-variant microscopy, the fluorescence microscope output is given by (see [9])

$$\tilde{s}(x, y, z; \boldsymbol{\theta}) = \int_{\tilde{z}} \int_{\tilde{y}} \int_{\tilde{x}} h(x - \tilde{x}, y - \tilde{y}, z, \tilde{z}) s(\tilde{x}, \tilde{y}, \tilde{z}; \boldsymbol{\theta}) \mathrm{d}\tilde{x} \mathrm{d}\tilde{y} \mathrm{d}\tilde{z}, \qquad (2.2)$$

where $h(x, y, z, \tilde{z})$ is the fluorescence microscope PSF for a point source at a depth $\tilde{z}$ in the QD illuminating object $s(\tilde{x}, \tilde{y}, \tilde{z}; \boldsymbol{\theta})$.

We group the measurements into a vector form:

$$\boldsymbol{g} = \tilde{\boldsymbol{s}} + \boldsymbol{w}_{\mathrm{P}} + \boldsymbol{w}_{\mathrm{b}}, \qquad (2.3)$$

where $\boldsymbol{g}$, $\tilde{\boldsymbol{s}}$, $\boldsymbol{w}_{\mathrm{P}}$, and $\boldsymbol{w}_{\mathrm{b}}$ are $(KLM \times 1)$–dimensional vectors whose $(KL((z - z_1)/\Delta z) + K((y - y_1)/\Delta y) + ((x - x_1)/\Delta x) + 1)^{\mathrm{th}}$ components are $g(\cdot)$, $\tilde{s}(\cdot)$, $w_{\mathrm{P}}(\cdot)$, and $w_{\mathrm{b}}(\cdot)$, respectively; $\Delta x = (x_{k+1} - x_k)$ with $k \in \{1, 2, \ldots K - 1\}$ and similarly for Δy and Δz.

---

[1]Note that the background noise considered in this chapter is an approximation, as there exist other types of background noise, e.g., electronic noise, readout noise, and quantization noise [18]. In principle, these latter types of background noise could be avoided using external control. However, in any case the thermal noise is the dominant component, it depends on the sensor material and increases with the sensor operating temperature [19].

Object Model (Nanosphere QD Intensity Profile of Two Neighboring Microspheres)

For the statistical design, we compute the error in estimating the target concentrations of two neighboring microspheres as a function of their distance and the temperature in their image sensing. Recall from Section 2.1.2 that the target concentrations on the microspheres are proportional to the intensity levels of the spherical-shell lights surrounding them. Consider two such shells $s_{\text{sh}}(x, y, z; \boldsymbol{\theta}_1)$ and $s_{\text{sh}}(x - d, y, z; \boldsymbol{\theta}_2)$ with unknown parameters $\boldsymbol{\theta}_1$ and $\boldsymbol{\theta}_2$, respectively, corresponding to the concentrations of the targets surrounding two neighboring microspheres with a distance d apart. We model the object as

$$s(x, y, z; \boldsymbol{\theta}) = s_{\text{sh}}(x, y, z; \boldsymbol{\theta}_1) + s_{\text{sh}}(x - d, y, z; \boldsymbol{\theta}_2) \tag{2.4}$$

with unknown parameters $\boldsymbol{\theta} = [\boldsymbol{\theta}_1^T, \boldsymbol{\theta}_2^T]^T$. Below we consider two different models to define $s_{\text{sh}}(\cdot)$, where the microspheres are either fully or partially covered with the targets. The full shell corresponds to cases where the target concentration is high, and/or the time period of the sensing is sufficiently long. The sparse shell corresponds to low target concentrations and/or short sensing durations.

• Full-shell model for $s_{\text{sh}}(\cdot)$: For a microsphere fully covered with the captured target molecules, the emitted nanosphere QD lights completely surround the microsphere, and result in a spherical shell source with known radii r_1 and r_2 as follows:

$$s_{\text{sh}}(x, y, z; \theta_i) = \begin{cases} \theta_i & \text{if } r_1 \leq \sqrt{x^2 + y^2 + z^2} \leq r_2, \\ 0 & \text{otherwise,} \end{cases} \tag{2.5}$$

where θ_i is the unknown intensity level which is constant in the shell and $i \in \{1, 2\}$ indexes two neighboring microspheres; see Figure 2.2(a) (right) where the color level signifies the target concentration [5].

We define the prior distribution of the unknown parameter θ_i for the ith shell ($\forall$ $i \in \{1, 2\}$) using a uniform distribution:

$$\theta_i \sim \mathcal{U}(0, \theta_{\text{MAX}}), \tag{2.6}$$

where $\mathcal{U}(0, \theta_{\text{MAX}})$ is a uniform random variable, distributed from zero to a known maximum value θ_{MAX} [20]. We assume that the prior distributions of θ_i for $i \in \{1, 2\}$ are statistically independent of each other. We adopt a uniform distribution prior for θ_i, since no additional information other than the maximum value of the target-concentration level is available in general.

• Sparse-shell model for $s_{\text{sh}}(\cdot)$: Here we consider a sparse model to describe the nanosphere QD light-intensity profile for cases where the microspheres are surrounded only partially with targets. In such cases, the target molecules are likely to be attached to each microsphere without fully covering it, and hence the resulting QD intensity profile $s_{\text{sh}}(\cdot)$ is sparse:

$$s_{\text{sh}}(x, y, z; \boldsymbol{\theta}_i) = \begin{cases} \theta_i(x, y, z) & \text{if } r_1 \le \sqrt{x^2 + y^2 + z^2} \le r_2, \\ 0 & \text{otherwise,} \end{cases} \tag{2.7}$$

where $\theta_i(x, y, z)$ is the unknown intensity level which is sparse in each measured voxel of the shell, and $i \in \{1, 2\}$ indexes two neighboring microspheres; see Figure 2.2(b) (right) where the color level in the figure signifies the target concentration [5]. For the ith shell ($\forall\ i \in \{1, 2\}$), we assume that the total number of voxels, where the

measurements are captured, is n_i. We denote the values of $\theta_i(\cdot)$ at these voxels are $\theta_{i1}, \theta_{i2}, \ldots, \theta_{in_i}$, which we stack in an n_i dimensional vector $\boldsymbol{\theta}_i = [\theta_{i1}, \theta_{i2}, \ldots, \theta_{in_i}]^T$.

We define the prior distribution of the unknown parameter θ_{ij} for the ith shell ($\forall$ $i \in \{1, 2\}$) at its jth measured voxel ($\forall$ $j \in \{1, 2, \ldots, n_i\}$) using an exponential distribution:

$$\theta_{ij} \sim \text{Exp}(\tau), \tag{2.8}$$

where $\text{Exp}(\tau)$ is an exponential random variable, with a scale parameter τ [20]. We assume that the prior distributions of θ_{ij} for $i \in \{1, 2\}$ and $j \in \{1, 2, \ldots, n_i\}$ are statistically independent of each other. Here the exponential distribution prior imposes a sparsity in θ_{ij}, and the parameter τ of this distribution inversely controls the sparsity level of θ_{ij}. Namely, a very small value of τ in (2.8) restricts the value of θ_{ij} to be very close to zero, and thus constrains θ_{ij} to be sparse. Note that a good knowledge of τ is important for solving the corresponding sparse parameter estimation problem using the prior model (2.8). If not known, one can attempt to estimate this parameter from the measurements in some way, and thus the resulting sparse parameter estimation method becomes completely free of user parameters [21], [22]. Note also that a Laplace distribution prior is widely used in the literature to define the prior distribution of sparse parameters, for solving maximum *a posteriori* (MAP) estimation problems [23]. However in our work, since θ_{ij} is positive, we define the prior distribution of this parameter using an exponential distribution prior instead of a Laplace distribution prior. Intuitively, the probability density function (pdf) along the positive axis of a Laplace distribution with zero location parameter value and the pdf of an exponential distribution are similar.
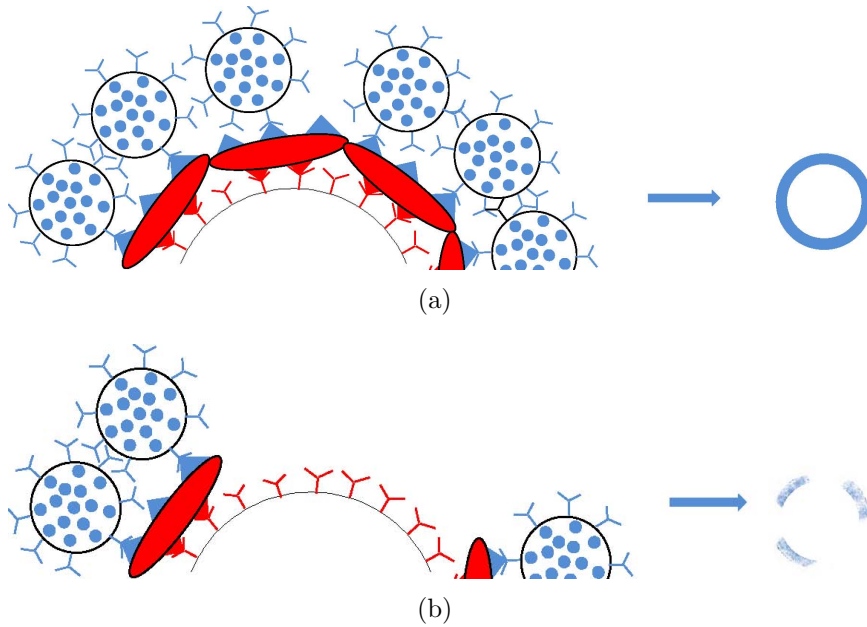
Figure 2.2: Left: Schematic of cross-section depicting target molecules captured (a) fully or (b) partially by a microsphere, and sandwiched by nanospheres, see the (a) full-shell and (b) sparse-shell models for $s_{\text{sh}}(\cdot)$. Right: Ideal cross-section ring intensity image of the resulting (a) full shell or (b) sparse shell, associated with the nanosphere quantum-dot lights. We schematize the left- and right-column figures of (a) and (b) without consistent scaling.

PSF Model

The fluorescence microscope typically distorts the 3D object image [11], [24]-[26]. We describe this distortion using the classical model in [9], which allows us compute the known PSF using the microscope imaging parameters following the manufacturer's specification. This model is

$$
h(x, y, z, \tilde{z}) = \left| \int_0^1 J_0(2\pi N_a \alpha \sqrt{x^2 + y^2}/M'\lambda) \exp(j2\pi\psi(z, \tilde{z}, N_a, \alpha, n_o, n_s)/\lambda)\alpha d\alpha \right|^2,
$$

$$(2.9)$$

where J_0 is the Bessel function of the first kind, N_a the microscope numerical aperture, α the normalized radius in the back focal plane, M' the lens magnification, λ the QD emission wavelength. Further

$$
\psi(\cdot) = n_o z \left[1 - (N_a\alpha/n_o)^2 \right]^{1/2} + n_s\tilde{z}\left\{ \left[1 - (N_a\alpha/n_o)^2 \right]^{1/2} - (n_o/n_s)^2 \left[1 - (N_a\alpha/n_o)^2 \right]^{1/2} \right\}
$$

$$(2.10)$$

is the optical path difference function. Moreover, n_o and n_s are the refractive indexes of the immersion oil and the specimen, respectively, and $\tilde{z}$ is the depth at which the point source is located in the object.

2.2.2 Posterior Cramér-Rao Bound

We compute the PCRB on the error in estimating the unknown parameters of (2.1) to optimize the design. We employ PCRB instead of CRB, as PCRB permits us to use realistic prior knowledge of the target-concentration levels for the proposed design. Namely, PCRB allows us to exploit the positivity information of the light-intensity level for the full-shell model (2.5) or the sparse-shell model (2.7), to constrain the

15

target-concentration level from zero to a known maximum value for the full-shell model (2.5), and to exploit the sparsity information of the target-concentration level for the sparse-shell model (2.7). Below, we first briefly discuss the concept of the PCRB. We then introduce the joint likelihood of the measurement and unknown parameters. After that we present the expressions of the elements of the (Fisher) information matrix, which we use to compute the PCRB.

PCRB

Let $\boldsymbol{g}$ represents a vector of the measured data, $\boldsymbol{\theta} = [\theta_1, \theta_2, \ldots, \theta_n]^T$ be an n dimensional unknown random parameter to be estimated, $p_{\boldsymbol{G},\boldsymbol{\Theta}}(\boldsymbol{g}, \boldsymbol{\theta})$ be the joint probability density of the pair $(\boldsymbol{g}, \boldsymbol{\theta})$, and $\boldsymbol{q}(\boldsymbol{g})$ is an estimate of $\boldsymbol{\theta}$, which is a function of $\boldsymbol{g}$. The PCRB on the estimation error has the form

$$\boldsymbol{Q} = \mathrm{E}\Big[[\boldsymbol{q}(\boldsymbol{g}) - \boldsymbol{\theta}][\boldsymbol{q}(\boldsymbol{g}) - \boldsymbol{\theta}]^T\Big] \geq \boldsymbol{J}^{-1}, \tag{2.11}$$

where $\mathrm{E}(\cdot)$ denotes the statistical expectation with respect to the joint pdf $p_{\boldsymbol{G},\boldsymbol{\Theta}}(\boldsymbol{g}, \boldsymbol{\theta})$ and $\boldsymbol{J}$ is the $n \times n$ (Fisher) information matrix with the elements

$$J_{i'j'} = \mathrm{E}\left[-\frac{\partial^2 \log p_{\boldsymbol{G},\boldsymbol{\Theta}}(\boldsymbol{g}, \boldsymbol{\theta})}{\partial \theta_{i'} \partial \theta_{j'}}\right], \qquad i', j' = 1, \ldots, n, \tag{2.12}$$

provided that the derivatives $\left(\frac{\partial^2 (\cdot)}{\partial \theta_{i'} \partial \theta_{j'}}\right)$ and $\mathrm{E}(\cdot)$ in (2.11) and (2.12) exist. The inequality in (2.11) means that the difference $\boldsymbol{Q} - \boldsymbol{J}^{-1}$ is a positive semidefinite matrix. We compute the PCRBs on the errors in estimating the unknown random parameters in $\boldsymbol{\theta}$ corresponding to the diagonal elements of $\boldsymbol{J}^{-1}$ [10], [27].

16

Joint Likelihood Function

The joint likelihood function of the measurement $\boldsymbol{g}$ and the unknown random parameter $\boldsymbol{\theta}$ using (2.1) is

$$p_{G,\Theta}(\boldsymbol{g}, \boldsymbol{\theta}) = p_{G|\Theta}(\boldsymbol{g}|\boldsymbol{\theta})p_{\Theta}(\boldsymbol{\theta}), \tag{2.13}$$

where $p_{G|\Theta}(\boldsymbol{g}|\boldsymbol{\theta})$ is the conditional pdf of $\boldsymbol{g}$ given $\boldsymbol{\theta}$ and $p_{\Theta}(\boldsymbol{\theta})$ is the marginal pdf of $\boldsymbol{\theta}$.

• Expression of $p_{G|\Theta}(\boldsymbol{g}|\boldsymbol{\theta})$:

$$p_{G|\Theta}(\boldsymbol{g}|\boldsymbol{\theta}) = \frac{1}{\sqrt{(2\pi)^{KLM}|\boldsymbol{\Sigma}_g|}} \exp\left[-\frac{1}{2}(\boldsymbol{g} - \tilde{\boldsymbol{s}})^T \boldsymbol{\Sigma}_g^{-1}(\boldsymbol{g} - \tilde{\boldsymbol{s}}) \right], \tag{2.14}$$

where $\boldsymbol{\Sigma}_g$ is the covariance matrix of $\boldsymbol{g}$. The expression of $\boldsymbol{\Sigma}_g$ is given by

$$\boldsymbol{\Sigma}_g = \frac{\text{diag}(\tilde{\boldsymbol{s}})}{\beta} + \sigma_{\text{b}}^2\boldsymbol{I}, \tag{2.15}$$

where $\text{diag}(\tilde{\boldsymbol{s}})$ denotes a diagonal matrix formed by the elements of $\tilde{\boldsymbol{s}}$ and $\boldsymbol{I}$ is an identity matrix of dimension KLM.

• Expression of $p_{\Theta}(\boldsymbol{\theta})$ for the full-shell model (2.5):

$$p_{\Theta}(\boldsymbol{\theta}) = \prod_{i=1}^{2} p_{\Theta_i}(\theta_i), \tag{2.16}$$

where $p_{\Theta_i}(\theta_i)$ is the prior pdf of the unknown parameter θ_i for the ith shell ($i \in \{1, 2\}$). Recall from Section 2.2.1 that θ_i follows a uniform distribution prior with a range from 0 to θ_{MAX}, see (2.6). Also note $\boldsymbol{\theta} = [\theta_1, \theta_2]^T$ with $n = 2$ is the unknown random parameter to be estimated for the full-shell case.

• Expression of $p_{\Theta}(\boldsymbol{\theta})$ for the sparse-shell model (2.7):

$$p_{\Theta}(\boldsymbol{\theta}) = \prod_{i=1}^{2}\prod_{j=1}^{n_i} p_{\Theta_{ij}}(\theta_{ij}), \tag{2.17}$$

where $p_{\Theta_{ij}}(\theta_{ij})$ is the prior pdf of the unknown parameter θ_{ij} for the ith shell ($i \in \{1, 2\}$) at its jth measured voxel ($\forall\, j \in \{1, 2, \ldots, n_i\}$). Recall from Section 2.2.1 that θ_{ij} follows an exponential distribution prior with a scale parameter τ, see (2.8). Also note $\boldsymbol{\theta} = [\theta_1, \theta_2, \ldots, \theta_{n1}, |\theta_{n1+1}, \ldots, \theta_n]^T = [\theta_{11}, \theta_{12}, \ldots, \theta_{1n_1}, |\theta_{21}, \theta_{22}, \ldots, \theta_{2n_2}]^T$ with $n = n_1 + n_2$ is the unknown random parameter to be estimated for the sparse-shell case.

Information Matrix

We derive the elements of the (Fisher) information matrix $\boldsymbol{J}$ using (2.12) for computing the PCRBs on the error in estimating the unknown random parameters in $\boldsymbol{\theta}$. Below we present the expressions of these elements for both the object models.

• (Fisher) information matrix for the full-shell model: Here we consider that the object model $s(\cdot)$ in (2.4) is formed using the full-shell model in (2.5). Recall that the unknown random parameter for the statistical design using the full-shell model is $\boldsymbol{\theta} = [\theta_1, \theta_2]^T$, see Sections 2.2.1 and (2.16).

We define

$$s_1(x, y, z) = \frac{\partial s(\cdot)}{\partial \theta_1} = \begin{cases} 1 & \text{if } r_1 \leq \sqrt{x^2 + y^2 + z^2} \leq r_2, \\ 0 & \text{otherwise}, \end{cases} \tag{2.18}$$

and

$$s_2(x,y,z) = \frac{\partial s(\cdot)}{\partial \theta_2} = \begin{cases} 1 & \text{if } r_1 \le \sqrt{(x-d)^2 + y^2 + z^2} \le r_2, \\ 0 & \text{otherwise.} \end{cases} \qquad (2.19)$$

Using (2.18) and (2.19), we further define

$$\tilde{s}_{i'}(x,y,z) = \int_{\tilde{z}} \int_{\tilde{y}} \int_{\tilde{x}} h(x-\tilde{x}, y-\tilde{y}, z, \tilde{z}) s_{i'}(\tilde{x}, \tilde{y}, \tilde{z}) \mathrm{d}\tilde{x} \mathrm{d}\tilde{y} \mathrm{d}\tilde{z}, \qquad i' \in \{1,2\}. \quad (2.20)$$

The expressions of the elements of the 2×2 symmetric matrix $\boldsymbol{J}$ using (2.20) are

$$J_{i'j'} = \mathrm{E}_{\boldsymbol{\theta}} \left[\sum_z \sum_y \sum_x \left(\frac{\tilde{s}_{i'}(\cdot)\tilde{s}_{j'}(\cdot)}{\left((\tilde{s}(\cdot)/\beta) + \sigma_{\mathrm{b}}^2\right)} + \frac{(\tilde{s}_{i'}(\cdot)/\beta)(\tilde{s}_{j'}(\cdot)/\beta)}{2\left((\tilde{s}(\cdot)/\beta) + \sigma_{\mathrm{b}}^2\right)^2} \right) \right], \qquad i', j' = 1, 2,$$

$$(2.21)$$

where we compute $\mathrm{E}_{\boldsymbol{\theta}}[\cdot]$ with respect to the pdf $p_{\boldsymbol{\Theta}}(\boldsymbol{\theta})$ in (2.16) using the Monte-Carlo integration estimation technique [28], see Appendix A.

• (Fisher) information matrix for the sparse-shell model: Here we consider that the object model $s(\cdot)$ in (2.4) is formed using the sparse-shell model in (2.7). Recall that the unknown random parameter for the statistical design using the sparse-shell model is $\boldsymbol{\theta} = [\theta_1, \theta_2, \dots, \theta_n]^T$, see Sections 2.2.1 and (2.17).

We assume that the measured voxel of $s(\cdot)$, that corresponds to the i'^{th} element $(i' \in \{1, 2, \dots, n\})$ of $\boldsymbol{\theta}$, is $\{x = x_k, y = y_l, z = z_m\}$, where $k \in \{1, 2, \dots, K\}$, $l \in \{1, 2, \dots, L\}$, and $m \in \{1, 2, \dots, M\}$. Using this assumption, we define

$$s_{i'}(x,y,z) = \frac{\partial s(\cdot)}{\partial \theta_{i'}} = \begin{cases} 1 & \text{if } x = x_k, y = y_l, z = z_m, \\ 0 & \text{otherwise.} \end{cases} \qquad (2.22)$$

19

We follow similar assumption and definition corresponding to the each element of $\boldsymbol{\theta}$. We then redefine $\tilde{s}_{i'}(x, y, z)$ for the sparse-shell case for $i' \in \{1, 2, \ldots, n\}$ by inserting $s_{i'}(x, y, z)$ from (2.22) in (2.20).

The expressions of the elements of the $n \times n$ symmetric matrix $\boldsymbol{J}$ using (2.20) are

$$
J_{i'j'} = \left(\frac{1}{\beta} - \frac{1}{2\beta^2} \right) \mathrm{E}_{\boldsymbol{\theta}} \left[\sum_z \sum_y \sum_x \left(\frac{\tilde{s}_{i'}(\cdot)\tilde{s}_{j'}(\cdot)}{\left((\tilde{s}(\cdot)/\beta) + \sigma_{\mathrm{b}}^2 \right)^2} \right) \right], \qquad i', j' = 1, 2, \ldots, n,
$$
(2.23)

where we compute $\mathrm{E}_{\boldsymbol{\theta}}[\cdot]$ with respect to the pdf $p_{\boldsymbol{\Theta}}(\boldsymbol{\theta})$ in (2.17) using the Monte-Carlo integration estimation technique [28], see Appendix A.

Comment

The expression of $J_{i'j'}$ in (2.21) or (2.23) involves computing $\mathrm{E}_{\boldsymbol{\theta}} \left[-\frac{\partial^2 \log p_{\boldsymbol{\Theta}}(\boldsymbol{\theta})}{\partial \theta_{i'}^2} \right]$ for $i' \in \{1, 2, \ldots, n\}$. Here the second derivative of $\log p_{\boldsymbol{\Theta}}(\boldsymbol{\theta})$ with respect to $\theta_{i'}$ does not exist at the boundary points of the prior pdf $p_{\Theta_{i'}}(\theta_{i'})$. However, the integral here with respect to $p_{\boldsymbol{\Theta}}(\boldsymbol{\theta})$, in computing the statistical expectation, is zero for almost surely at the boundary points of $p_{\Theta_{i'}}(\theta_{i'})$. This is because the probability measure of the prior pdfs at each of their boundary point is zero, as the prior pdfs are continuous in our analysis. Thus, we arbitrarily include or exclude the boundary points of the prior pdfs in the computation, and assume that the second derivative of $\log p_{\boldsymbol{\Theta}}(\boldsymbol{\theta})$ with respect to $\theta_{i'}$ exists for almost surely with probability one on the set of points where the prior pdfs are non-zero [29].

2.3 Statistical Design

We present our statistical design method for selecting the optimal (minimal) distance between the microspheres as well as the optimal operating temperature in their image sensing. We first present the performance measure for the design as a function of distance and temperature. We then present a least-squares (LS) estimation algorithm for automatically selecting the minimal distance from the performance measure at a given temperature [30]. We thereafter discuss how we select the optimal operating temperature.

2.3.1 Performance Measure

We define the performance measure in estimating the target concentrations as the sum of the PCRBs on the errors in estimating the target concentrations. Namely, we define the performance measure as

$$p = \text{tr(PCRB)}, \tag{2.24}$$

where "tr" is the matrix trace operation and PCRB $= \boldsymbol{J}^{-1}$ [31]-[33]. We compute this measure as a function of the design variables, i.e., the distance d between the microspheres and the operating temperature T of the image sensor. From our discussion so far, it is evident that p is a function of d, see Section 2.2. Below we discuss the relationship between this measure with T.

The performance measure p is a function of the noise level σ_b^2, see (2.1), which in turn is a function of T. Thus, p is a function of T. Specifically,

$$\sigma_b^2(T) = B \exp(-E_g/2k_B T), \tag{2.25}$$

where B is a constant, E_g is the known bandgap of the image-sensor material, and k_B is the known Boltzmann constant [19]. Here we assume B is known; otherwise, we estimate it using images captured from a training experiment, see Section 2.4. We further assume that E_g is constant for a given image sensor material, although E_g varies with T in reality. In this chapter, we consider the image sensor material is Silicon (Si), and the relationship between E_g with T for Si (see, e.g., [34]) is

$$E_g = 1.15 - \frac{7.3021 \times 10^{-4} T^2}{1108 + T}, \tag{2.26}$$

where the T dependent second term is negligible for the temperature range that we use in the numerical examples presented in Sections 2.5.2 and 2.5.3 to illustrate the concept of our proposed design. Hence, we consider E_g is constant and its value to be 1.15 in this chapter. Note that one should replace E_g in (2.26) and consider its temperature dependency based on the choice of the image sensor material of interest.

2.3.2   Minimal Distance Selection

We compute the minimal distance by analyzing p as a function of the distance d between the microspheres at a given temperature, to obtain a desired error in estimating the target concentrations. We conduct an LS estimation to automatically select the minimal distance. Below we first discuss our motivation to conduct the estimation

for the minimal distance selection, and we then discuss the corresponding analysis details. Here we use $p(d)$ to denote p as a function of d.

Motivation

Intuitively, as we increase the distance between the microspheres, the light signals from their nanosphere QDs do not interfere with each other. Thus, $p(d)$ flattens, see Figure 2.3(a), and the error in estimating the target concentrations is essentially due to the background noise in each microsphere location individually. In other words, the errors between the microspheres are decoupled, and the PCRB matrix should be block diagonal. Thus, we could automatically estimate the minimal distance from $p(d)$ corresponding to the distance at which such a decoupling occurs.

To estimate at what distance $p(d)$ starts to flatten, we first replace in $p(d)$ the ML estimates of B and β. (See in Section 2.4 a discussion on the ML estimation.) We denote this estimated $p(d)$ as $\tilde{p}(d)$. We then fit with $\tilde{p}(d)$ a parametric curve, that models the shape of $\tilde{p}(d)$ as a function of d, using an LS estimation. The LS estimate of the distance at which $\tilde{p}(d)$ starts to flatten should be the minimal distance estimate.

Parametric Shape Model of $\tilde{p}(d)$

We propose a parametric curve to model the shape of $\tilde{p}(d)$; see Figure 2.3(a) which essentially resembles the shape of $\tilde{p}(d)$. This model is given by

$$p'(d) = c \exp(\rho d)\mathcal{I}_{[0,d_0)}(d) + p_0, \tag{2.27}$$

where c, ρ, d_0, and p_0 are the unknown parameters, and $\mathcal{I}_{[0,d_0)}(d)$ is an indicator function given by,

$$\mathcal{I}_{[0,d_0)}(d) = \begin{cases} 1 & \text{if } 0 \leq d < d_0, \\ 0 & \text{otherwise.} \end{cases} \tag{2.28}$$

Similar to $\tilde{p}(d)$, here $p'(d)$ in (2.27) first decreases as d increases, and it then starts to flatten from $d = d_0$; see Figure 2.3(b) for an illustrative example.

(a)   (b)
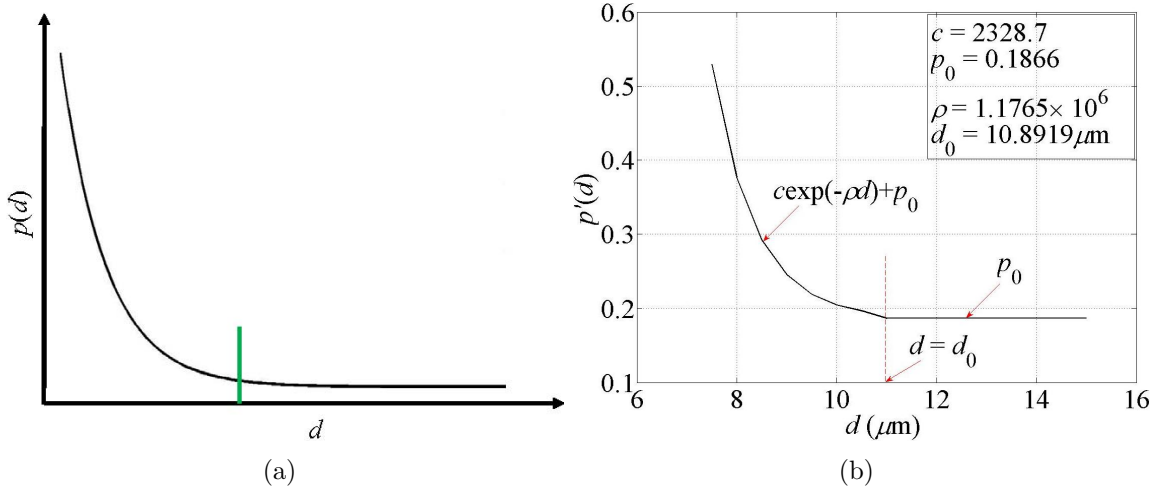
Figure 2.3: (a) Schematic diagram of $p(d)$. (b) Graph example of the proposed parametric model $p'(d)$ that represents $p(d)$ shape. Similar to $p(d)$, this graph first decreases as d increases, and it then starts to flatten from d_0.

Minimal Distance Estimation Using Least-Squares

We estimate d_0 using an LS estimation method. Namely, we first compute $\tilde{p}(d)$ at N increasing values of d at $d_1 \leq d_2 \leq \ldots \leq d_N$, and we then fit these computed values with $p'(d)$ computed at $d_1, d_2, \ldots, d_N$. The relationship between $\tilde{p}(d)$ and $p'(d)$ in a matrix-vector form is given by

$$\tilde{\boldsymbol{p}} = \boldsymbol{p}' + \boldsymbol{e}, \tag{2.29}$$

24

where $\tilde{\boldsymbol{p}} = [\tilde{p}(d_1), \tilde{p}(d_2), \ldots, \tilde{p}(d_N)]^T$, $\boldsymbol{p}' = [p'(d_1), p'(d_2), \ldots, p'(d_N)]^T$, and $\boldsymbol{e}$ is the error vector. We rewrite (2.29) further as

$$\tilde{\boldsymbol{p}} = \boldsymbol{A}(\boldsymbol{\zeta})\boldsymbol{x} + \boldsymbol{e}, \tag{2.30}$$

where $\boldsymbol{A}(\boldsymbol{\zeta})$ is an $N \times 2$ dimensional matrix with k'^{th} row ($k' \in \{1, 2, \ldots, N\}$) as $[\exp(-\rho d_{k'})\mathcal{I}_{[0,d_0)}(d_{k'}), 1]$, $\boldsymbol{\zeta} = [\rho, d_0]^T$, and $\boldsymbol{x} = [c, p_0]^T$.

The least-squares estimates of the unknown parameters (see, e.g., [30]) are

$$
\begin{aligned}
\widehat{\boldsymbol{\zeta}} &= \arg\max_{\boldsymbol{\zeta}}\{\tilde{\boldsymbol{p}}^T\boldsymbol{\Pi}(\boldsymbol{\zeta})\tilde{\boldsymbol{p}}\}, \\
\widehat{\boldsymbol{x}} &= [\boldsymbol{A}^T(\widehat{\boldsymbol{\zeta}})\boldsymbol{A}(\widehat{\boldsymbol{\zeta}})]^{-1}\boldsymbol{A}^T(\widehat{\boldsymbol{\zeta}})\tilde{\boldsymbol{p}},
\end{aligned}
\tag{2.31}
$$

where argmax stands for the argument of the maximum, i.e., the value of the given argument $\boldsymbol{\zeta}$ for which the value of the expression $\tilde{\boldsymbol{p}}^T\boldsymbol{\Pi}(\boldsymbol{\zeta})\tilde{\boldsymbol{p}}$ attains its maximum value, and $\boldsymbol{\Pi}(\boldsymbol{\zeta})$ is the projection matrix on the column space of $\boldsymbol{A}(\boldsymbol{\zeta})$ [30], given as

$$\boldsymbol{\Pi}(\boldsymbol{\zeta}) = \boldsymbol{A}(\boldsymbol{\zeta})[\boldsymbol{A}^T(\boldsymbol{\zeta})\boldsymbol{A}(\boldsymbol{\zeta})]^{-1}\boldsymbol{A}^T(\boldsymbol{\zeta}). \tag{2.32}$$

We select the minimal distance d_{opt} as

$$d_{\text{opt}} = \widehat{d_0}. \tag{2.33}$$

2.3.3   Optimal Operating Temperature Selection

We select the optimal operating temperature T_{opt} by analyzing p as a function of the temperature T in image sensing, to obtain a desired accuracy in estimating the target

concentrations. Namely, we select the T_{opt} that ensures a desired performance through p for all possible distances between the microspheres; see more details in Sections 2.5.2 and 2.5.3. The ability to select the optimal operating temperature using the performance analysis is critical for employing less expensive sensors, while attaining a desired estimation accuracy, see Sections 2.1.2, 2.5.2, and 2.5.3. Specifically, we choose the optimal operating temperature as a trade off between less cooling (i.e., reducing the device cost) vs. higher estimation accuracy.

2.4 Estimating β and B Using an Existing 3D Microarray

In this section, we estimate β and B, which we use for the statistical design, using a training experiment that we conduct with the existing 3D microarray layout. Namely, we image using the desired image sensor the lights generated by the QDs embedded in $\tilde{N}$ number of target-free microspheres placed randomly on a substrate [6]. We estimate β using a method-of-moments (MoM) estimation method [30] from each microsphere image, and estimate B from the noise-only section of the captured image. The estimate of β from one microsphere image to the other varies in general, see Section 2.5.1. Hence, we use a large $\tilde{N}$ number of microsphere images, estimate β from each of them, and substitute the statistical median of these estimates to replace β for the statistical design described in Section 2.3. (We discuss in Section 2.5.1 our motivation of using the statistical median of the β estimates instead of their statistical mean for the design.) Below we first describe the measurement model for fluorescence microscopy imaging of a target-free microsphere embedded with QDs. We then present our proposed analysis to estimate β and B.

2.4.1   Measurement Model

Here we employ the measurement model (2.1), assuming that the object $s(x, y, z; \boldsymbol{\gamma})$ with unknown parameter $\boldsymbol{\gamma}$ is the QD light-intensity profile of a single microsphere, and assuming also that β and B are the other unknown parameters. We rewrite the measurement model as

$$g(x, y, z; \boldsymbol{\gamma}, \beta, B) = \tilde{s}(x, y, z; \boldsymbol{\gamma}) + w_{\text{p}}(x, y, z; \boldsymbol{\gamma}, \beta) + w_{\text{b}}(x, y, z; B), \qquad (2.34)$$

where $x \in \{x_1, x_2, \ldots, x_K\}$, $y \in \{y_1, y_2, \ldots, y_L\}$, and $z \in \{z_1, z_2, \ldots, z_M\}$; and $(x_{k+1} - x_k) = \Delta x$ ($\forall \ k = 1$ to $(K-1)$). We make similar assumptions for Δy and Δz.

• Object Model (Microsphere QD Intensity Profile): We model this intensity profile using a parametric sphere of constant intensity level θ per voxel [15]. Namely, we define

$$s(x, y, z; \boldsymbol{\gamma}) = \begin{cases} \theta & \text{if} \quad \sqrt{(x - x_{\text{c}})^2 + (y - y_{\text{c}})^2 + (z - z_{\text{c}})^2} \ \leq r, \\ 0 & \text{otherwise}, \end{cases} \qquad (2.35)$$

where θ denotes the unknown average intensity level which is constant in the sphere, x_{c}, y_{c}, and z_{c} are the unknown center location parameters, and r is the known radius of the microsphere. We denote the unknown parameter vector of the object by $\boldsymbol{\gamma} = [\theta, x_{\text{c}}, y_{\text{c}}, z_{\text{c}}]^T$; see also Section 3.2.1 for a more detailed discussion.

For simplicity, we assume a constant intensity level at every microsphere voxel. Intuitively, this assumption is justified because the QDs are typically tightly and uniformly packed inside each microsphere [6]; they produce light at nm resolution, whereas the

microscope measurement is done at μm resolution. Note that more complex models here could be used to obtain more realistic results tailored to specific applications.

2.4.2 Estimation

In this part, we present our proposed procedure for estimating β and B, using the captured image from a training experiment, see Section 2.5.1. Below, we first propose an MoM estimation method [30] for estimating β in (2.34) from each microsphere image. This estimation needs the estimates of B and γ. Therefore, we present next how we estimate B. We then briefly review our parametric ML estimation method [15] for estimating the object parameter γ in (2.34) from each microsphere image; see also Chapter 3.

Estimating β

The reciprocal photon-conversion factor β for fluorescence microscopy is determined by several physical parameters, such as the integration time and the quantum efficiency of the detector [25], which are unknown in our research. Hence, we estimate β in (2.34) using an MoM estimation method [30] from each microsphere image. This estimate is (see Appendix B) given by

$$\hat{\beta} = \frac{\sum_z \sum_y \sum_x \tilde{s}(x,y,z;\hat{\gamma})}{\sum_z \sum_y \sum_x \left[\left(g(x,y,z) - \tilde{s}(x,y,z;\hat{\gamma}) \right)^2 - \widehat{\sigma_{\mathrm{b}}^2} \right]}, \tag{2.36}$$

where $\hat{\gamma}$ is the estimate of the object parameter from the corresponding microsphere image, and $\widehat{\sigma_{\mathrm{b}}^2}$ is the estimate of the background noise variance in the captured image, see (2.37). We denote the estimates of β from the $\tilde{N}$ number of microsphere images

28

as $\hat{\beta}_1, \hat{\beta}_2, \ldots, \hat{\beta}_{\tilde{N}}$. We substitute the statistical median of these estimates to replace β for the statistical design analysis described in Section 2.3; see also Section 2.5.1 for more details.

Estimating B

We estimate B from the noise-only section of the captured image. Recall that the background noise $w_{\mathrm{b}}(x, y, z; B)$ in the captured-image is a zero-mean Gaussian noise with variance σ_{b}^2, and is iid from voxel to voxel, see Section 2.2.1. Recall also that σ_{b}^2 is related to B following (2.25). We thus estimate first σ_{b}^2 from the noise-only section of the captured image using the classical ML estimation method discussed in [35, Ch. 6]. We estimate then B as

$$\hat{B} = \frac{\widehat{\sigma_{\mathrm{b}}^2}}{\exp(-E_{\mathrm{g}}/2k_{\mathrm{B}}T_0)}, \tag{2.37}$$

where $\widehat{\sigma_{\mathrm{b}}^2}$ is the estimate of σ_{b}^2 and T_0 is the temperature at which the image is captured in the training experiment. Note that it is possible here to use sufficient number of measurement samples, and to ensure the estimate of B is consistent [30].

Estimating $\boldsymbol{\gamma}$

We estimate the object parameter $\boldsymbol{\gamma}$ from each microsphere image. Here we assume a large β, since we employ an image sensor with high sensitivity, see Section 2.1.2. We also assume the contribution of $w_{\mathrm{P}}(x, y, z; \boldsymbol{\gamma}, \beta)$ is negligible in (2.34), since the QD light imaging is a high signal-to-noise ratio (SNR) imaging [5]. Thus, estimating $\boldsymbol{\gamma}$ is essentially equivalent to fitting $\tilde{s}(x, y, z; \boldsymbol{\gamma})$ to the available measurement $g(x, y, z; \boldsymbol{\gamma})$

29

of a single microsphere at each voxel of the measurement. Therefore, we approximate (2.34) as follows:

$$g(x, y, z; \boldsymbol{\gamma}) = \tilde{s}(x, y, z; \boldsymbol{\gamma}) + w_{\mathrm{b}}(x, y, z). \qquad (2.38)$$

Considering, $\boldsymbol{\eta} = [x_{\mathrm{c}}, y_{\mathrm{c}}, z_{\mathrm{c}}]^T$ and defining $\tilde{s}'(x, y, z; \boldsymbol{\eta}) = \tilde{s}(\cdot)/\theta$, we rewrite (2.38) as

$$g(x, y, z; \boldsymbol{\gamma}) = \theta \tilde{s}'(x, y, z; \boldsymbol{\eta}) + w_{\mathrm{b}}(x, y, z). \qquad (2.39)$$

With these assumptions and notations, we group the measurements into a vector form:

$$\boldsymbol{g} = \theta \tilde{\boldsymbol{s}}'(\boldsymbol{\eta}) + \boldsymbol{w}_{\mathrm{b}}, \qquad (2.40)$$

where $\boldsymbol{g}$, $\tilde{\boldsymbol{s}}'(\boldsymbol{\eta})$, and $\boldsymbol{w}_{\mathrm{b}}$ are $(KLM \times 1)$–dimensional vectors whose $(KL((z - z_1)/\Delta z) + K((y - y_1)/\Delta y) + ((x - x_1)/\Delta x) + 1)^{\mathrm{th}}$ components are $g(\cdot)$, $\tilde{s}'(\cdot)$, and $w_{\mathrm{b}}(\cdot)$ respectively. The log-likelihood function for estimating $\boldsymbol{\gamma}$ using (2.40) is given by

$$C(\boldsymbol{\gamma}) \approx -||\boldsymbol{g} - \theta \tilde{\boldsymbol{s}}'(\boldsymbol{\eta})||^2, \qquad (2.41)$$

where $|| \cdot ||^2$ denotes the Euclidean vector-norm operation[2].

The ML estimate of the parameters (see, e.g., [36]) is

$$\begin{aligned} \hat{\boldsymbol{\eta}} &= \arg \max_{\boldsymbol{\eta}} \{\boldsymbol{g}^T \boldsymbol{P}_{\tilde{s}'}(\boldsymbol{\eta}) \boldsymbol{g}\}, \\ \hat{\theta} &= [\tilde{\boldsymbol{s}}'^T(\hat{\boldsymbol{\eta}}) \tilde{\boldsymbol{s}}'(\hat{\boldsymbol{\eta}})]^{-1} \tilde{\boldsymbol{s}}'^T(\hat{\boldsymbol{\eta}}) \boldsymbol{g}, \end{aligned} \qquad (2.42)$$

---

[2] For a vector $\boldsymbol{x} = [x_1, x_2, \ldots, x_{n'}]^T$, the Euclidean norm is $||x|| = \sqrt{x_1^2 + x_2^2 \ldots + x_{n'}^2}$ [37].

where $\boldsymbol{P}_{\tilde{s}'}(\boldsymbol{\eta})$ is the projection matrix on the column space of $\tilde{\boldsymbol{s}}'(\boldsymbol{\eta})$ [30], given as

$$\boldsymbol{P}_{\tilde{s}'}(\boldsymbol{\eta}) = \tilde{\boldsymbol{s}}'(\boldsymbol{\eta})[\tilde{\boldsymbol{s}}'^{T}(\boldsymbol{\eta})\tilde{\boldsymbol{s}}'(\boldsymbol{\eta})]^{-1}\tilde{\boldsymbol{s}}'^{T}(\boldsymbol{\eta}). \tag{2.43}$$

We then denote the estimate of $\boldsymbol{\gamma}$ as $\hat{\boldsymbol{\gamma}} = [\hat{\theta}, \hat{\boldsymbol{\eta}}^{T}]^{T}$, which we use for estimating β in (2.36). See also Chapter 3 for a more general description of estimating the object parameter $\boldsymbol{\gamma}$ from fluorescence microscopy images of a single microsphere, embedded with QDs and placed randomly on a substrate.

2.5 Results

We present our results for statistically designing the proposed position-encoded 3D microarray. Recall that our statistical design analysis uses the values of the imaging parameters β and B. We estimate them from fluorescence microscopy images of $\tilde{N}$ number of target-free microspheres placed randomly on the substrate of the existing 3D microarray layout, see Sections 2.3 and 2.4. Thus, we first present our results in estimating β and B from these microsphere images. We then present two numerical examples to illustrate the concept of our proposed statistical design using the full- and sparse-shell models.

For the purpose of the illustration only, we consider in this chapter a Zeiss Axioscope 2 Mot+ fluorescence microscope [38] with an Axiocam MRm monochrome camera [39], to image the microsphere QD lights. However, our proposed statistical design analysis is general, and can be applicable in imaging the proposed microarray using any fluorescence microscope and any CCD or CMOS image sensor. In particular, one can

employ inexpensive image sensors produced by Watec Inc. [13] or Micron Inc. [14], which require temperature cooling in imaging, see Section 2.3.3.

2.5.1 Estimating β and B

In this part, we present our results in estimating β and B from fluorescence microscopy images of $\tilde{N}$ number of target-free microspheres placed randomly on a substrate. We first present the imaging experiment, and we then present our estimation results.

Imaging Experiment

We randomly placed target-free microspheres on a polydimethylsiloxane substrate. These microspheres are made of polystyrene, and have a refractive index of 1.334. They are QD-embedded, and are 5μm in diameter. They contain cadmium selenium sulphide QDs measuring 6nm in diameter [6]. The QDs were excited at wavelengths lower than 500nm using blue/UV lights [6].

To image the microsphere QD lights, we employed a 10X objective with the numerical aperture N_a of the microscope as 1.3, and used water as an immersion medium for the objective. We imaged the QD emission in 535nm wavelength at $T_0 = 10^0$C. We captured the 3D image with a resolution of $\Delta z = 1\mu$m along the z-direction, and $\Delta x = \Delta y = 0.654\mu$m/pixel along the lateral direction.

We show the focal-plane intensity image of all the microspheres in Figure 2.4(a). This image in Figure 2.4(a) illustrates optical cross-talk (as mentioned in Chapter 1) in the locations where the microsphere images bind in clusters. Naturally, the microsphere images are optically indistinguishable in these locations.

Results
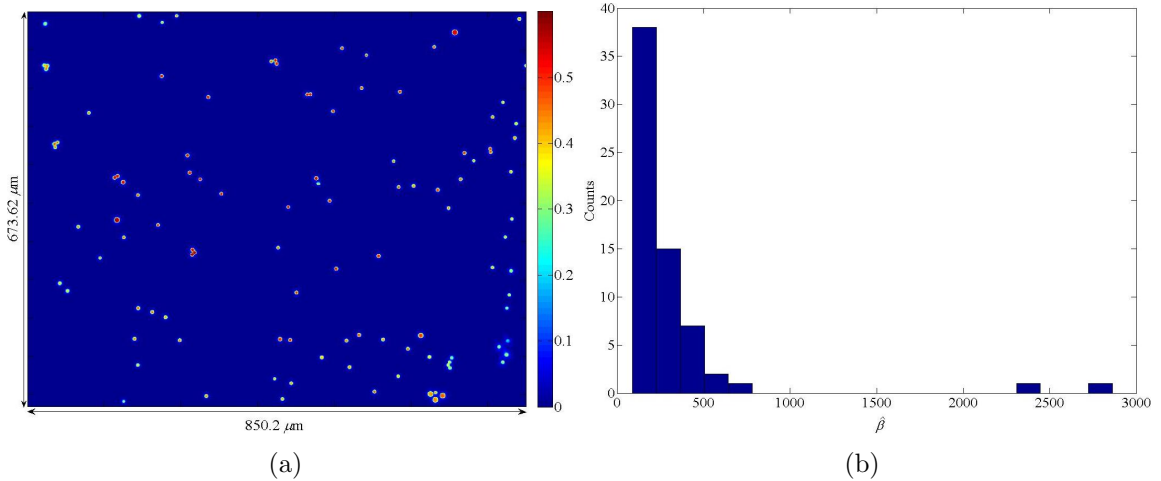
Figure 2.4: (a) Focal-plane quantum-dot intensity image of all the microspheres. (b) Histograms of the estimated β from the individual microsphere images.

In Figure 2.4(b), we present a histogram of the β estimates that we obtain from the image shown in Figure 2.4(a). We find 65 microsphere images appear as individual objects in Figure 2.4(a). We manually segment these images, and estimate β from each of them. We observe that the β estimates vary in Figure 2.4(b), and also note a few outliers in the histogram of their estimates. The presence of these outliers motivates us to use the statistical median of the β estimates for the statistical design, which we compute as 305.21. We also compute the statistical median of the θ estimates as 0.0053. (Recall that θ is the average QD intensity level of a microsphere, see (2.35).) We further compute $\widehat{\sigma_{\mathrm{b}}^2} = 4.23 \times 10^{-4}$ from the noise-only section of the image in Figure 2.4(a), and we then compute $\hat{B} = 7.29 \times 10^6$ using (2.37) and using $E_{\mathrm{g}} = 1.15\mathrm{eV}$, see Section 2.3.1. We substitute the values of the estimated B and the median of the estimated β to replace B and β in our proposed statistical design in the next two subsections. Moreover, we use the median of the estimated θ to decide

33

the value of θ_{MAX} in the numerical example below for the statistical design using the full-shell models; see Section 2.5.2 for more details.

2.5.2 Example 1: Statistical Design for the Full-Shell Case

In this example, we illustrate the concept of our proposed statistical design of the position-encoded 3D microarrays for the full-shell models. Here we use the shell radii $r_1 = 2.774\mu$m and $r_2 = 2.874\mu$m in (2.5) for protein targets of diameter 250nm. We compute these radii by considering the respective sizes of the microspheres, nanospheres, and bio-receptors (e.g., IgG antibody), which are 5μm, 100-200nm, and 10-12nm in diameter, respectively. We also use the order of θ_{MAX} in (2.6) is similar as the median of the θ estimates in Section 2.5.1. Note that the choice of θ_{MAX} is not so critical here, as we show below that the statistical design is robust with respect to θ_{MAX}.

Effect of Microspheres' Distance on Performance

In Figure 2.5(a), we present the effect of the microspheres' distance on the statistical imaging performance. Here we use $\theta_{\mathrm{MAX}} = 0.0053$ and $T = 0^0$C. We observe that the estimated performance measure $\tilde{p}(d)$ first decreases as d increases, and it then flattens. This result is similar with what we intuitively predict in Section 2.3.2 on the shape of $\tilde{p}(d)$ as a function of d. We estimate using the proposed LS estimation method (see Section 2.3.2) the distance at which $\tilde{p}(d)$ starts to flatten. Recall that we define this distance as the minimal distance between the microspheres in our proposed statistical design analysis, see Section 2.3.2. In this example, we estimate the minimal distance to be 17μm.
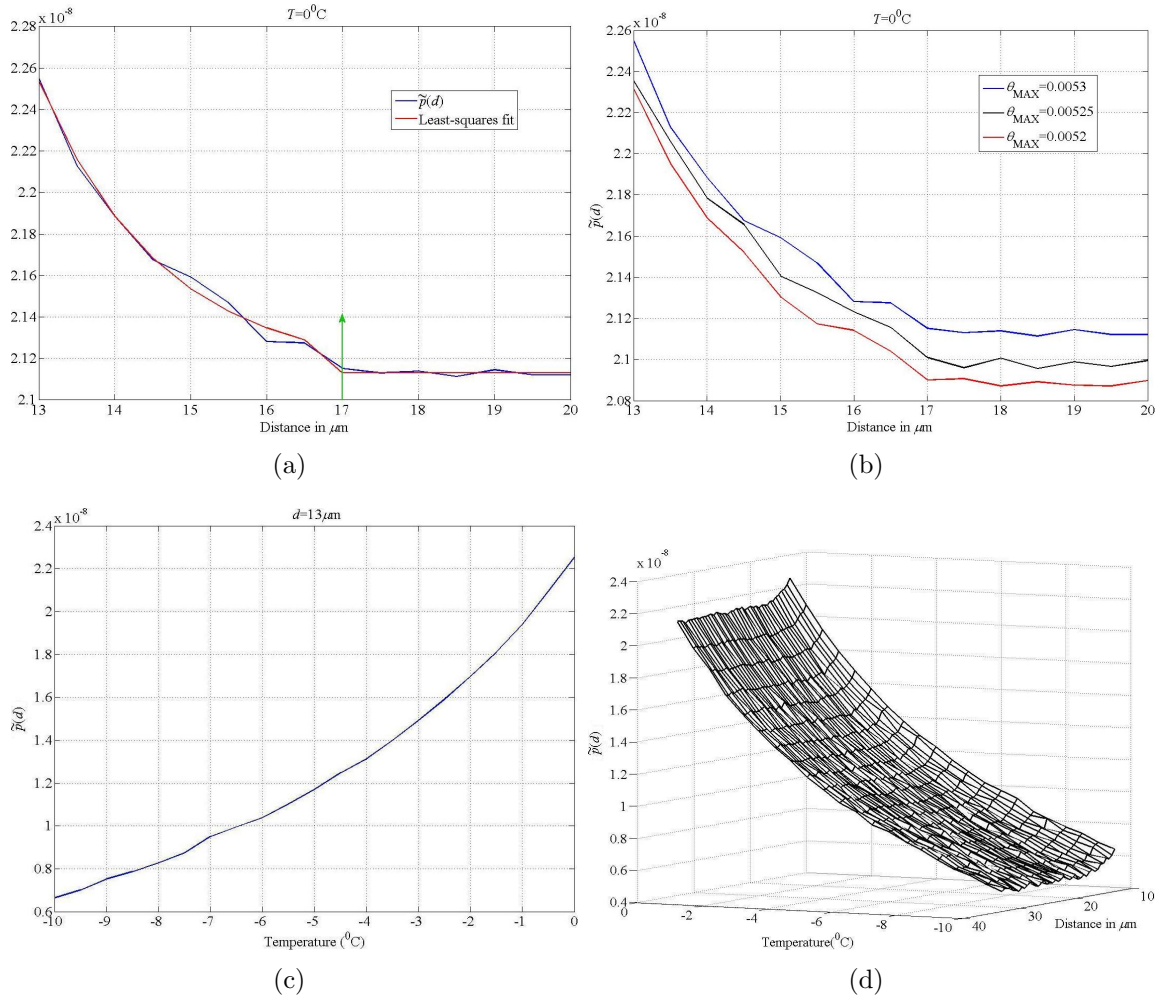
Figure 2.5: Design results for the full-shell models, see Section 2.5.2. (a) Minimal distance is 17μm. (b) Design at 0^0C for varying θ_{MAX}. (c) Design at $d = 13\mu$m. (d) Performance as a function of temperature and distance.

Effect of Maximum Light Level on Design

In Figure 2.5(b), we present the effect of the maximum microsphere light level θ_{MAX} on the statistical design performance. Here we use $\theta_{\mathrm{MAX}} = 0.0053$, 0.00525, and 0.0052, and $T = 0^0$C. We qualitatively observe that the minimal distance does not change with varying θ_{MAX}. This result suggests that the minimal distance is robust with respect to the maximum possible target-concentration level.

Effect of Temperature on Performance

In Figure 2.5(c), we present the effect of the imaging temperature on the statistical design performance. Here we use $\theta_{\mathrm{MAX}} = 0.0053$, and consider that the microspheres are very close to each other with a distance of 13μm. We observe that the performance degrades with higher temperature at a fixed distance. This result is useful to select the optimal operating temperature of the image sensor for the desired performance in imaging; see also Section 2.3.3.

Distance and Temperature Effects on Performance

In Figure 2.5(d), we present the effects of the microspheres' distance and the imaging temperature on the statistical design performance. Here we use $\theta_{\mathrm{MAX}} = 0.0053$. We qualitatively observe that the statistical design performance is more sensitive on the temperature in imaging than the distance between the microspheres, for the full-shell models.

2.5.3 Example 2: Statistical Design for the Sparse-Shell Case

We illustrate the concept of our proposed statistical design of the position-encoded 3D microarrays for the sparse-shell models. Here we use similar values for the shell radii r_1 and r_2 in (2.7) as we use in Example 1, and consider protein targets of diameter 250nm. We also use $\tau = 1$ and $\tau = 5$ in (2.8) for more sparsity and for less sparsity, respectively. Note that the choice of τ is not so critical here, as we show below that the statistical design is robust with respect to τ.

Effect of Microspheres' Distance on Performance

In Figure 2.6(a), we present the effect of the microspheres' distance on the statistical imaging performance. Here we use $\tau = 1$ and $T = 10^0$C. We observe that the estimated performance measure $\tilde{p}(d)$ first decreases as d increases, and it then flattens. This result is similar with what we obtain for the full-shell models in Example 1. We then compute the minimal distance to be 11μm following the same procedure that we employ in Example 1.

Effect of Sparsity on Design

In Figure 2.6(b), we present the effect of the sparsity on the statistical design performance. Here we use $\tau = 1$ and 5, and $T = -10^0$C. We qualitatively observe that the minimal distance does not change with varying τ. This result suggests that the minimal distance is robust with respect to the sparsity level.
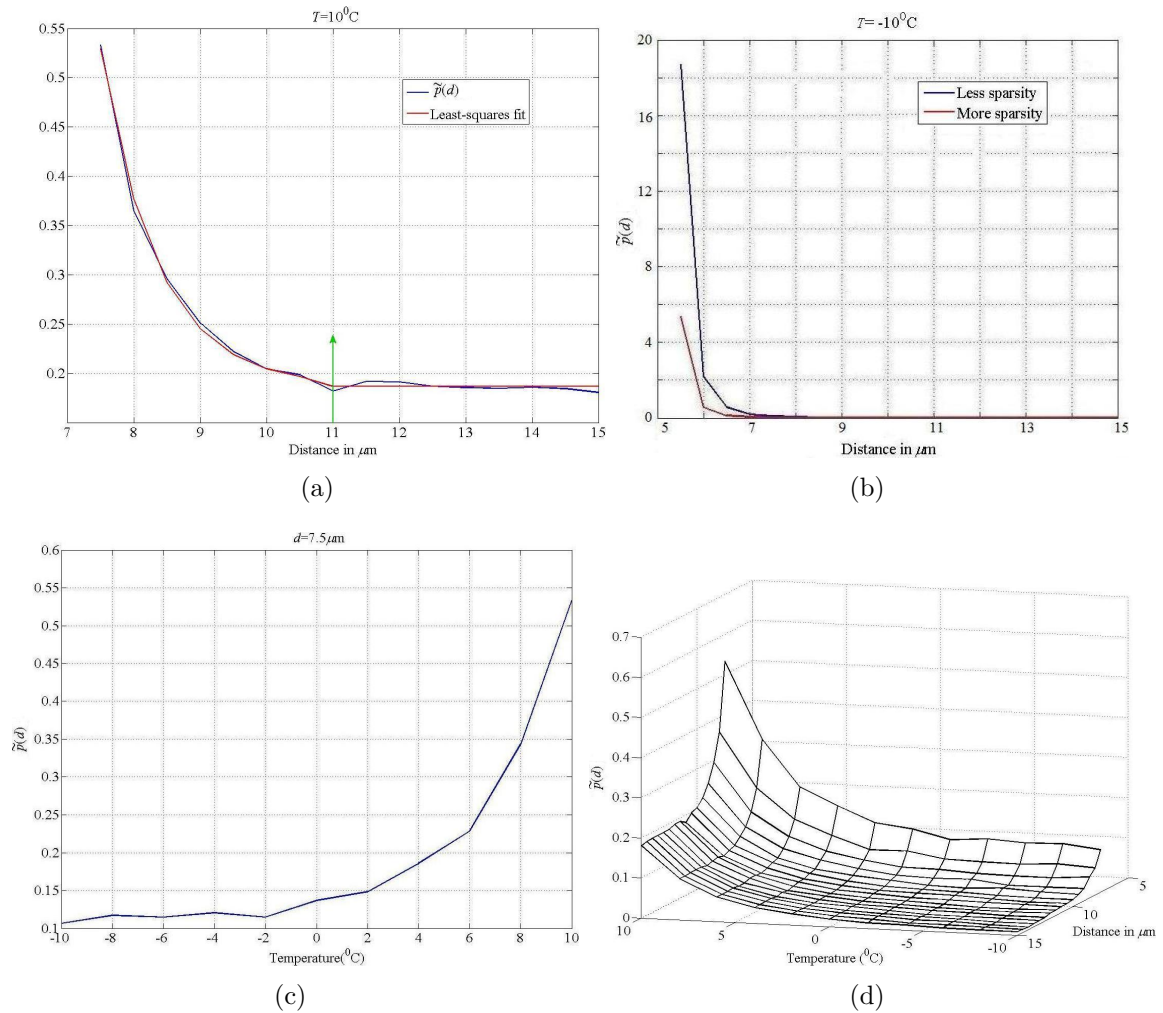
Figure 2.6: Design results for the sparse-shell models, see Section 2.5.3. (a) Minimal distance is 11μm. (b) Design at -10^0C with $\tau = 1$ (red) and $\tau = 5$ (blue). (c) Design at $d = 7.5\mu$m. (d) Performance as a function of temperature and distance.

Effect of Temperature on Performance

In Figure 2.6(c), we present the effect of the imaging temperature on the statistical design performance. Here we use $\tau = 1$, and consider similar to Example 1 that the microspheres are very close to each other with a distance of 7.5μm. In this set-up, we obtain a similar result that we obtain for the full-shell models in Example 1. Namely, we observe that the performance degrades with higher temperature at a fixed distance. Thus, similar to Example 1, we find the result here is useful to select the optimal operating temperature of the image sensor for the desired performance in imaging; see also Section 2.3.3.

Distance and Temperature Effects on Performance

In Figure 2.6(d), we present the effects of the microspheres' distance and the imaging temperature on the statistical design performance. Here we use $\tau = 1$. We qualitatively observe that the statistical design performance degrades with higher temperature and/or with closer distance between the microspheres.

Chapter 3

Estimating Intensity Levels and Locations of Quantum-Dot Embedded Microspheres[3]

In this chapter, we develop a parametric maximum likelihood (ML) method to estimate the intensity levels and locations of microspheres from their images. The microspheres are embedded with quantum-dots (QDs) and placed randomly on a substrate. The imaging is performed using a fluorescence microscope and an image sensor. We first describe our problem of interest and the pertinent measurement model, considering additive Gaussian noise. We assume here that the three-dimensional (3D) point-spread function (PSF) representing the microscope blurring is unknown, and model this PSF using a 3D Gaussian function for computational efficiency. Here, parametric spheres represent the microsphere light-intensity profiles. We then develop the estimation algorithm for single-sphere object images. The algorithm is tested numerically and compared with the analytical Cramér-Rao bound (CRB). To apply our analysis

---

[3]Based on "Estimating locations of quantum-dot–encoded microparticles from ultra-high density 3D microarrays," by P. Sarder and A. Nehorai, in *IEEE Trans. on NanoBioscience,* vol. 7, pp. 284-297, Dec. 2008. ©[2008] IEEE.

to real data, we first segment a section of the 3D image of multiple microspheres using a *k*-means clustering algorithm, obtaining images of single-sphere objects. Then each of these images is processed using our proposed estimation method.

Using numerical examples, we compare the performance of our proposed algorithm with the conventional blind-deconvolution (BD) algorithm embedded in MATLAB [7] and the parametric blind-deconvolution (PBD) algorithm [8]. Our algorithm outperforms these algorithms in high signal-to-noise ratio (SNR) images. It achieves the CRB at high SNR, as should be expected for the ML estimation methods; the other two do not. Our algorithm performs better, as it contains prior information of the object shape (spherical), whereas the other algorithms (BD and PBD) do not have that flexibility.

Comparing the performance of our proposed algorithm with the BD algorithm using real data, we observe that both algorithms perform similarly for microspheres that are well separated, whereas their performances differ for microspheres that are very close to each other.

This chapter is organized as follows. Section 3.1 briefly introduces the research problem. Section 3.2 presents the statistical measurement model. Section 3.3 discusses the proposed estimation method. Section 3.4 provides numerical examples. Finally, Section 3.5 shows results obtained from the real data.

3.1   Problem Description

In this section, after briefly discussing imaging nomenclature, we describe microsphere imaging and our goal.

41

3.1.1 Imaging Nomenclature
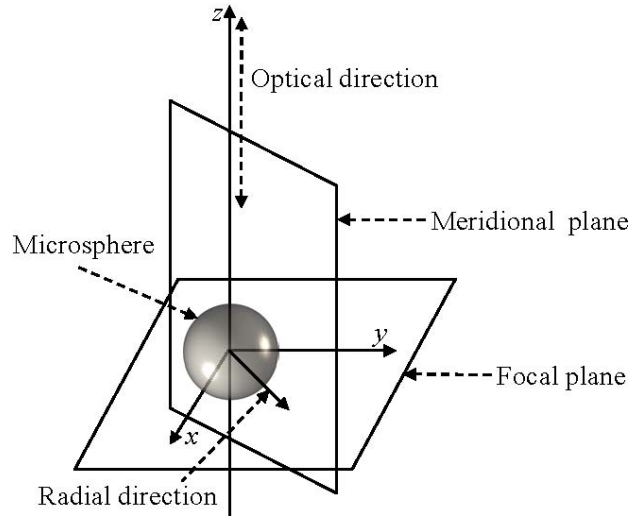
Figure 3.1: A schematic view of the focal plane, optical direction, radial direction, and meridional plane in the Cartesian coordinate system. The microsphere to be imaged is at the center of the coordinate axes.

In this chapter, we assume that the center of the microsphere to be imaged is the center of the Cartesian coordinate system shown in Figure 3.1. The z axis is the optical direction, and we capture the microsphere 3D image along this direction from a series of 2D focal-plane images. Any direction parallel to the focal plane is a radial direction. The plane along the optical direction, perpendicular to the focal plane and passing through the origin, is the meridional plane.

3.1.2 Imaging Microspheres

We image multiple microspheres, embedded with QDs and placed randomly on a substrate. Upon excitation by UV light, all the microsphere QDs emit light, and together resemble the form of a luminous sphere. The intensity levels of the microspheres proportionally varies with their QD concentrations; see Figure 3.2 (right) where the

color level signifies such a level [5]. To capture the image, a fluorescence microscope is focused at different depth planes of the microspheres, parallel to the xy plane in Figure 3.1. This produces a series of 2D cross-section images of lights emitted by the microsphere QDs [11]. Thus, each cross-section image of the sphere light formed in a microsphere forms the image of a disc whose diameter varies with the depth of the cross section. A cooled CCD with high sensitivity captures the 2D cross-section images, introducing almost negligible thermal noise in the captured images [40].
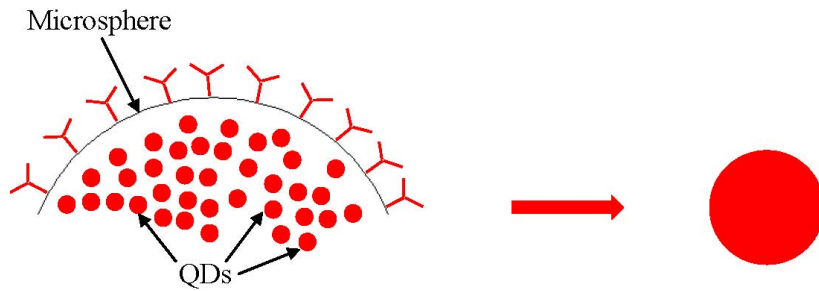
Figure 3.2: Left: Schematic of cross-section depicting a quantum-dot–embedded microsphere. Right: Ideal cross-section disc intensity image of the resulting sphere associated with the microsphere quantum-dot lights. We schematize the left- and right-column figures here without consistent scaling.
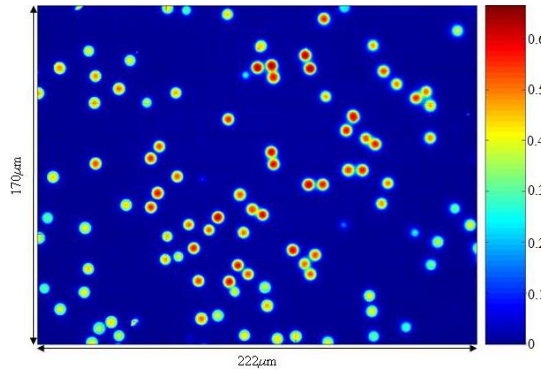
Figure 3.3: Focal-plane quantum-dot intensity of imaged microspheres. ©[2008] IEEE.

Figure 3.3 shows a focal-plane intensity image of multiple microspheres. Here, we seek to estimate the locations and intensity levels of these imaged microspheres, which are useful for the statistical design presented in Chapter 2.

3.2 Statistical Measurement Model

The measurement at the CCD output, in fluorescence microscopy imaging of a single QD-embedded microsphere is given by [15]:

$$g(x, y, z; \boldsymbol{\varphi}, \beta, \sigma_\mathrm{b}^2) = \tilde{s}(x, y, z; \boldsymbol{\varphi}) + w_\mathrm{P}(x, y, z; \boldsymbol{\varphi}, \beta) + w_\mathrm{b}(x, y, z; \sigma_\mathrm{b}^2), \qquad (3.1)$$

where $x \in \{x_1, x_2, \ldots, x_K\}$, $y \in \{y_1, y_2, \ldots, y_L\}$, and $z \in \{z_1, z_2, \ldots, z_M\}$; K, L, and M denote the numbers of measurement voxels; $\boldsymbol{\varphi}$ is the unknown parameter vector in imaging; $\tilde{s}(x, y, z; \boldsymbol{\varphi})$ is the microscope output; $w_\mathrm{P}(x, y, z; \boldsymbol{\varphi}, \beta)$ is a zero-mean Gaussian noise with variance $\tilde{s}(\cdot)/\beta$, and β is the reciprocal of the photon-conversion factor [16], [17], which is unknown; $w_\mathrm{P}(\cdot)$ models the interference due to the photon counting process in the CCD, and is independent from voxel to voxel; $w_\mathrm{b}(x, y, z; \sigma_\mathrm{b}^2)$ models the background noise, which is a zero-mean Gaussian noise with unknown variance σ_b^2; $w_\mathrm{b}(\cdot)$ is due to the thermal noise of the CCD [18], is independently and identically distributed (iid) from voxel to voxel, and is statistically independent with $w_\mathrm{P}(\cdot)$. Thus, $g(x, y, z; \boldsymbol{\varphi}, \beta, \sigma_\mathrm{b}^2)$ is Gaussian distributed with mean $\tilde{s}(\cdot)$ and variance $\tilde{s}(\cdot)/\beta + \sigma_\mathrm{b}^2$, independent from voxel to voxel [15]. In this chapter, we assume that the CCD output is free of constant offset [18].

Assuming a space-invariant microscopy, the microscope output is given by [11]

$$\tilde{s}(x, y, z; \boldsymbol{\varphi}) = s(x, y, z; \boldsymbol{\gamma}) \otimes h(x, y, z; \boldsymbol{\tau}), \qquad (3.2)$$

where $\boldsymbol{\varphi} = [\boldsymbol{\gamma}^T, \boldsymbol{\tau}^T]^T$, $\boldsymbol{\gamma}$ is the unknown parameter vector of the QD illuminating microsphere $s(x, y, z; \boldsymbol{\gamma})$, $\boldsymbol{\tau}$ is the unknown parameter vector of the microscope PSF $h(x, y, z; \boldsymbol{\tau})$, and $\otimes$ denotes the convolution operation [41].

We group the measurements into a vector form:

$$\boldsymbol{g} = \tilde{\boldsymbol{s}} + \boldsymbol{w}_{\mathrm{P}} + \boldsymbol{w}_{\mathrm{b}}, \qquad (3.3)$$

where $\boldsymbol{g}$, $\tilde{\boldsymbol{s}}$, $\boldsymbol{w}_{\mathrm{P}}$, and $\boldsymbol{w}_{\mathrm{b}}$ are $(KLM \times 1)$–dimensional vectors whose $(KL((z - z_1)/\Delta z) + K((y - y_1)/\Delta y) + ((x - x_1)/\Delta x) + 1)^{\mathrm{th}}$ components are $g(\cdot)$, $\tilde{s}(\cdot)$, $w_{\mathrm{P}}(\cdot)$, and $w_{\mathrm{b}}(\cdot)$, respectively; $\Delta x = (x_{k+1} - x_k)$ ($\forall \ k = 1$ to $(K - 1)$), and similarly for Δy and Δz.

3.2.1 Single-Sphere Object Model (Microsphere QD Intensity Profile)

We model the QD light-intensity profile of a microsphere using a parametric sphere as follows:

$$s(x, y, z; \boldsymbol{\gamma}) = \begin{cases} \theta & \text{if} \quad \sqrt{(x - x_{\mathrm{c}})^2 + (y - y_{\mathrm{c}})^2 + (z - z_{\mathrm{c}})^2} \ \le r, \\ 0 & \text{otherwise,} \end{cases} \qquad (3.4)$$

where θ denotes the unknown average intensity level, which is constant in the microsphere and is proportional to the number of QDs present inside the microsphere;

x_c, y_c, and z_c are the unknown center location parameters; and r is the known radius of the microsphere. We denote the unknown parameter vector of the object by $\boldsymbol{\gamma} = [\theta, x_c, y_c, z_c]^T$.

We assume here for simplicity a homogeneous intensity profile to model the object. This reduces the number of unknowns, and thus increases the computational efficiency of the parameter estimation algorithm discussed in Section 3.3. Also, employing an inhomogeneous intensity profile in (3.4) would result in an overly ill-posed estimation analysis, requiring additional prior information on the object intensity profile to achieve a desired performance. Intuitively, our assumption is justified, as the QDs are typically tightly and uniformly packed inside each microsphere [6]; they produce light at nm resolution, whereas the microscope measurement is done at μm resolution. Note that more complex models could be used here to obtain more realistic results tailored to specific applications.

3.2.2 Three-Dimensional Gaussian Point-Spread Function Model

The PSF is the 3D impulse response[4] of a fluorescence microscope used to characterize the out-of-focus light. Note that, in a fluorescence microscope, the 3D impulse response is not an exact 3D impulse [24]. Namely, the finite lens aperture of the microscope introduces diffraction ring patterns in its focal planes. In addition, its measurement set-up usually differs from the manufacturer's design specifications.

---

[4]A three-dimensional impulse response is the output intensity profile of a microscope when the input is a point light source in space; a 3D impulse. A 3D impulse represents the limiting case of a light pulse in space made very short in volume, while maintaining a finite volume integral, thus giving an infinitely high intensity peak [41].

Therefore, the microscope PSF becomes phase aberrated with symmetric features in the focal planes and with asymmetric features along the optical direction [11].

In general, a 3D PSF can be obtained by three different techniques: experimental, analytical, and computational [11]. In experimental methods, images of one or more point-like objects are collected and used to obtain the PSF. These methods have the advantage that the PSF closely matches the experimental set-up. However, images obtained with such point-like objects have a very poor SNR unless the system is specially optimized. In the analytical methods, the PSF is calculated using the classical model proposed in [9], see (3.5). In the computational methods, it is preferable to estimate the PSF and object simultaneously using BD algorithms [11]; see also Appendix C. Such is the case when all the PSF parameters are not known, or a PSF measurement is difficult to obtain.

The classical 3D PSF model for a fluorescence microscope (see, e.g., [9] and [42]) is

$$h(x, y, z; \boldsymbol{\phi}) = \left| \int_0^1 J_0(2\pi N_a \alpha \sqrt{x^2 + y^2}/M'\lambda) \exp(j2\pi\psi(z; \boldsymbol{\phi})/\lambda)\alpha \mathrm{d}\alpha \right|^2, \qquad (3.5)$$

where J_0 is the Bessel function of the first kind, N_a the microscope numerical aperture, α the normalized radius in the back focal plane, M' the lens magnification, λ the QD emission wavelength. Further, $\psi(\cdot)$ is the optical path difference function between the corresponding systems in design and non-design conditions. Moreover, the vector $\boldsymbol{\phi}$ contains the true and ideal measurement set-up parameters: the refractive indices of the immersion oil (n_o), specimen (n_s), and cover-slip (n_g); the thickness of the immersion oil (t_o) and coverslip (t_g); the distance between the back-focal and detector planes (z_d); and the depth $(\tilde{z})$ at which the point source is located in the specimen [9].

The PSF model (3.5) is computationally expensive, as the integration in the formula requires intensive numerical evaluation. We thus perform the estimation in this chapter using a 3D Gaussian PSF model proposed in [43]. This model is given by

$$h(x, y, z; \boldsymbol{\tau}) = A \exp \left(-\frac{x^2 + y^2}{2\sigma_1^2} - \frac{z^2}{2\sigma_2^2} \right), \tag{3.6}$$

where the unknown parameter vector is $\boldsymbol{\tau} = [\sigma_1^2, \sigma_2^2]^T$. The model (3.6) for representing the fluorescence microscope PSF assumes that the Gaussian functions are centered at the origin of the PSF and they are separable, where the origin in (3.5) and (3.6) is $\{x = 0, y = 0, z = 0\}$. The advantage of using this centered separable 3D Gaussian PSF model is that it preserves the symmetry and asymmetry of the classical PSF model in (3.5) along the focal planes and the optical direction, respectively. We further assume in our proposed estimation in Section 3.3 that the PSF model in (3.6) is normalized according to the L^∞ norm[5], and thus $A = 1$.

3.2.3 Verification of Single-Sphere Object and Gaussian Point-Spread Function Models

We verify here our proposed single-sphere object and the Gaussian PSF models. Namely, we use real data and present a simple illustration for this verification. We assume here that a blurred microsphere image shown in Figure 3.3 is analytically represented by the unknown object convolved by the unknown PSF with additive

---

[5]For a vector $\boldsymbol{x} = [x_1, x_2, \ldots, x_{n'}]^T$, the L^∞ norm is $\max(|x_1|, |x_2|, \ldots, |x_{n'}|)$ [37].

Gaussian noise [41]. Following this assumption, we apply the BD algorithm[6] embedded in MATLAB to a randomly chosen and manually segmented microsphere image, shown in Figure 3.4(a).

Figure 3.4(b) shows a meridional section of the resulting estimated intensity profile of the object. This profile resembles a sphere, and thus justifies our proposed single-sphere object model. Note that the BD-estimated intensity profile of the object does not give a precise estimate of the microsphere center. We thus use an analytical estimation method to fit our proposed single-sphere object model (3.4) to the statistical measurement model (3.1) for estimating the microsphere center.

Figure 3.4(c) shows a meridional section of the resulting BD-estimated PSF that we obtain by applying the BD algorithm to the microsphere image shown in Figure 3.4(a). This profile resembles a Gaussian shape, and justifies the Gaussian PSF model (3.6). Furthermore, to visualize the similarity between the BD-estimated PSF and the PSF from the Gaussian PSF model (3.6), we use a least-squares fit [30], and show the meridional section of the resultant estimate in Figure 3.4(d). We compute here the least-squares error as 4.42%, and thus confirm that we do not lose much in estimation accuracy using the PSF model (3.6).

3.3   Estimation

We develop an ML method to estimate the unknown parameters φ from the captured 3D image segment of a microsphere. In this section, we first describe our proposed

---

[6]We use the *deconvblind* command of MATLAB, with an initial PSF represented by ones in all the voxels, to run the BD algorithm in this chapter. As described in Appendix C, this algorithm follows the conventional blind-deconvolution method [18], [44].
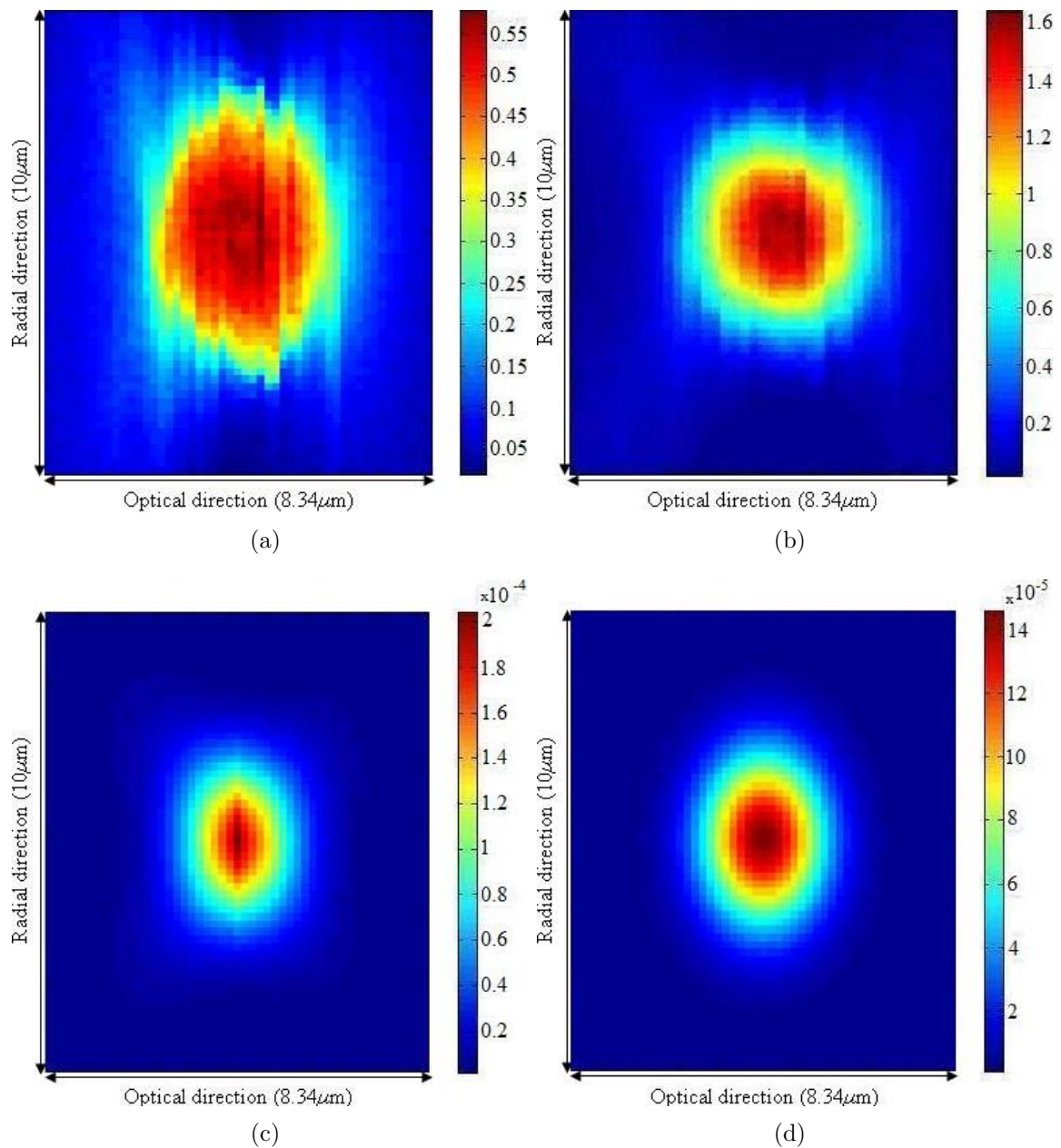
Figure 3.4: Meridional sections of (a) a microsphere intensity profile and (b) the resulting blind-deconvolution–estimated object intensity profile. Meridional sections of (c) the blind-deconvolution–estimated point-spread function intensity profile from the microsphere intensity profile shown in Figure 3.4(a) and (d) its least-squares fitted version using the model (3.6). ©[2008] IEEE.

estimation method considering an unknown 3D Gaussian PSF. We then compute the CRB, which is the lowest bound on the variance of the error of any unbiased estimator of the parameters in $\boldsymbol{\varphi}$ under certain regularity conditions [30].

The likelihood of $g(\cdot)$ in (3.1) for a measured voxel (see Section 3.2) is

$$C'(\boldsymbol{\varphi}, \beta, \sigma_\mathrm{b}^2) = \frac{1}{\sqrt{2\pi(\tilde{s}(\cdot; \boldsymbol{\varphi})/\beta + \sigma_\mathrm{b}^2)}} \exp\left[-\frac{(g(\cdot; \boldsymbol{\varphi}, \beta, \sigma_\mathrm{b}^2) - \tilde{s}(\cdot; \boldsymbol{\varphi}))^2}{2(\tilde{s}(\cdot; \boldsymbol{\varphi})/\beta + \sigma_\mathrm{b}^2)} \right]. \qquad (3.7)$$

We assume β and σ_b^2 are known, and estimate $\boldsymbol{\varphi}$ as follows,

$$\begin{aligned}
\widehat{\boldsymbol{\varphi}} &= \arg\min_{\boldsymbol{\varphi}} \ln(\tilde{s}(\cdot; \boldsymbol{\varphi})/\beta + \sigma_\mathrm{b}^2) + \frac{(g(\cdot; \boldsymbol{\varphi}, \beta, \sigma_\mathrm{b}^2) - \tilde{s}(\cdot; \boldsymbol{\varphi}))^2}{(\tilde{s}(\cdot; \boldsymbol{\varphi})/\beta + \sigma_\mathrm{b}^2)} \qquad (3.8) \\
&= \arg\min_{\boldsymbol{\varphi}} \tilde{C}'(\boldsymbol{\varphi}, \beta, \sigma_\mathrm{b}^2),
\end{aligned}$$

where argmin stands for the argument of the minimum, i.e., the value of the given argument $\boldsymbol{\varphi}$ for which the value of the expression $\tilde{C}'(\boldsymbol{\varphi}, \beta, \sigma_\mathrm{b}^2)$ attains its minimum value.

We differentiate $\tilde{C}'(\cdot)$ with respect to $\boldsymbol{\varphi}$, equate the resultant expression with zero, and obtain,

$$\frac{\mathrm{d}\tilde{s}(\cdot; \boldsymbol{\varphi})}{\mathrm{d}\boldsymbol{\varphi}} \left[\frac{1}{\beta(\tilde{s}(\cdot; \boldsymbol{\varphi})/\beta + \sigma_\mathrm{b}^2)} - \frac{2(g(\cdot; \boldsymbol{\varphi}, \beta, \sigma_\mathrm{b}^2) - \tilde{s}(\cdot; \boldsymbol{\varphi}))}{(\tilde{s}(\cdot; \boldsymbol{\varphi})/\beta + \sigma_\mathrm{b}^2)} - \frac{(g(\cdot; \boldsymbol{\varphi}, \beta, \sigma_\mathrm{b}^2) - \tilde{s}(\cdot; \boldsymbol{\varphi}))^2}{\beta(\tilde{s}(\cdot; \boldsymbol{\varphi})/\beta + \sigma_\mathrm{b}^2)^2} \right] = 0.$$
$$(3.9)$$

Simplifying (3.9), we obtain

$$\beta\tilde{s}^2(\cdot; \boldsymbol{\varphi}) + (1 + 2\sigma_\mathrm{b}^2\beta^2)\tilde{s}(\cdot; \boldsymbol{\varphi}) + \beta(\sigma_\mathrm{b}^2 - g^2(\cdot; \boldsymbol{\varphi}, \beta, \sigma_\mathrm{b}^2) - 2\sigma_\mathrm{b}^2\beta g(\cdot; \boldsymbol{\varphi}, \beta, \sigma_\mathrm{b}^2)) = 0. \quad (3.10)$$

We represent here (3.10) in a quadratic form of

$$a'\tilde{s}^2(\cdot;\boldsymbol{\varphi}) + b'\tilde{s}(\cdot;\boldsymbol{\varphi}) + c' = 0, \tag{3.11}$$

where

$$
\begin{aligned}
a' &= \beta, \\
b' &= 1 + 2\sigma_{\mathrm{b}}^2\beta^2, \\
c' &= \beta(\sigma_{\mathrm{b}}^2 - g^2(\cdot;\boldsymbol{\varphi},\beta,\sigma_{\mathrm{b}}^2) - 2\sigma_{\mathrm{b}}^2\beta g(\cdot;\boldsymbol{\varphi},\beta,\sigma_{\mathrm{b}}^2)).
\end{aligned}
\tag{3.12}
$$

Since, $\tilde{s}(\cdot)$ is always positive, a unique solution to (3.10) for estimating $\boldsymbol{\varphi}$ exists when

$$
\begin{aligned}
b'^2 - 4a'c' &> 0, \\
a'c' &< 0.
\end{aligned}
\tag{3.13}
$$

We compute

$$b'^2 - 4a'c' = 1 + 4(\sigma_{\mathrm{b}}^2\beta^2 + \beta g(\cdot))^2 > 0, \tag{3.14}$$

which satisfies $b'^2 - 4a'c' > 0$. To satisfy $a'c' < 0$, we require

$$\sigma_{\mathrm{b}}^2 > \max\left(0, \frac{-g^2(\cdot)}{2\beta g(\cdot) - 1}\right), \tag{3.15}$$

which is valid in our research because we capture microsphere images using a CCD with high sensitivity, i.e., a CCD with a large β, see Section 3.1.2, and we capture the images at a high SNR, as the QD light imaging is a high SNR imaging [5]. Thus, we prove that a unique solution to (3.10) exists.

We solve (3.10), and obtain

$$\widehat{\tilde{s}(\cdot;\boldsymbol{\varphi})} = \frac{-(1+2\sigma_{\mathrm{b}}^2\beta^2) + \sqrt{1+4(\sigma_{\mathrm{b}}^2\beta^2 + \beta g(\cdot;\boldsymbol{\varphi},\beta,\sigma_{\mathrm{b}}^2))^2}}{2\beta}. \tag{3.16}$$

We approximate $1 + 4(\sigma_{\mathrm{b}}^2\beta^2 + \beta g(\cdot))^2 \sim 4(\sigma_{\mathrm{b}}^2\beta^2 + \beta g(\cdot))^2$, and thus we have

$$\widehat{\tilde{l}(\cdot;\boldsymbol{\varphi})} = \left(g(\cdot;\boldsymbol{\varphi},\beta,\sigma_{\mathrm{b}}^2) - \frac{1}{2\beta}\right) \sim g(\cdot). \tag{3.17}$$

The approximations in (3.16)-(3.17) here are applicable for high SNR imaging and for large β, and thus they are valid in our work.

The relationship in (3.17) suggests that the estimation of $\boldsymbol{\varphi}$ is essentially equivalent to fitting $\tilde{s}(\cdot;\boldsymbol{\varphi})$ to the available measurement $g(\cdot)$ for each measured voxel. We thus ignore the effect of $w_{\mathrm{p}}(\cdot)$, and approximate (3.1) as follows:

$$g(x,y,z;\boldsymbol{\varphi},\sigma_{\mathrm{b}}^2) = \tilde{s}(x,y,z;\boldsymbol{\varphi}) + w_{\mathrm{b}}(x,y,z,\sigma_{\mathrm{b}}^2). \tag{3.18}$$

Considering $\boldsymbol{\eta} = [x_{\mathrm{c}}, y_{\mathrm{c}}, z_{\mathrm{c}}, \boldsymbol{\tau}^T]^T$, and defining $\tilde{s}'(x,y,z;\boldsymbol{\eta}) = \tilde{s}(\cdot)/\theta$, we rewrite (3.18) as

$$g(x,y,z;\boldsymbol{\varphi},\sigma_{\mathrm{b}}^2) = \theta\tilde{s}'(x,y,z;\boldsymbol{\eta}) + w_{\mathrm{b}}(x,y,z;\sigma_{\mathrm{b}}^2). \tag{3.19}$$

With these assumptions and notations, we group the measurements into a vector form:

$$\boldsymbol{g} = \theta\tilde{\boldsymbol{s}}'(\boldsymbol{\eta}) + \boldsymbol{w}_{\mathrm{b}}, \tag{3.20}$$

where $\boldsymbol{g}$, $\tilde{\boldsymbol{s}}'(\boldsymbol{\eta})$, and $\boldsymbol{w}_{\mathrm{b}}$ are $(KLM \times 1)$–dimensional vectors whose $(KL((z - z_1)/\Delta z) + K((y - y_1)/\Delta y) + ((x - x_1)/\Delta x) + 1)^{\mathrm{th}}$ components are $g(\cdot)$, $\tilde{s}'(\cdot)$, and $w_{\mathrm{b}}(\cdot)$ respectively. The log-likelihood function for estimating $\boldsymbol{\varphi}$ using (3.20) is given by

$$C(\boldsymbol{\varphi}, \sigma_{\mathrm{b}}^2) = -\frac{KLM}{2} \ln \sigma_{\mathrm{b}}^2 - \frac{||\boldsymbol{g} - \theta \tilde{\boldsymbol{s}}'(\boldsymbol{\eta})||^2}{2\sigma_{\mathrm{b}}^2}, \tag{3.21}$$

where $|| \cdot ||^2$ denotes the Euclidean vector-norm operation.

The ML estimate of the parameters (see, e.g., [36]) is

$$\begin{aligned}
\hat{\boldsymbol{\eta}} &= \arg\max_{\boldsymbol{\eta}} \{\boldsymbol{g}^T \boldsymbol{P}_{\tilde{s}'}(\boldsymbol{\eta}) \boldsymbol{g}\}, \\
\hat{\theta} &= [\tilde{\boldsymbol{s}}'^T(\hat{\boldsymbol{\eta}}) \tilde{\boldsymbol{s}}'(\hat{\boldsymbol{\eta}})]^{-1} \tilde{\boldsymbol{s}}'^T(\hat{\boldsymbol{\eta}}) \boldsymbol{g}, \\
\widehat{\sigma_{\mathrm{b}}^2} &= (KLM)^{-1} \boldsymbol{g}^T \boldsymbol{P}_{\tilde{s}'}^{\perp}(\boldsymbol{\eta}) \boldsymbol{g}, \tag{3.22}
\end{aligned}$$

where $\boldsymbol{P}_{\tilde{s}'}(\boldsymbol{\eta})$ is the projection matrix on the column space of $\tilde{\boldsymbol{s}}'(\boldsymbol{\eta})$, and $\boldsymbol{P}_{\tilde{s}'}^{\perp}(\boldsymbol{\eta})$ is the complementary projection matrix [30], given as

$$\begin{aligned}
\boldsymbol{P}_{\tilde{s}'}(\boldsymbol{\eta}) &= \tilde{\boldsymbol{s}}'(\boldsymbol{\eta})[\tilde{\boldsymbol{s}}'^T(\boldsymbol{\eta}) \tilde{\boldsymbol{s}}'(\boldsymbol{\eta})]^{-1} \tilde{\boldsymbol{s}}'^T(\boldsymbol{\eta}), \\
\boldsymbol{P}_{\tilde{s}'}^{\perp}(\boldsymbol{\eta}) &= \boldsymbol{I} - \boldsymbol{P}_{\tilde{s}'}(\boldsymbol{\eta}), \tag{3.23}
\end{aligned}$$

where $\boldsymbol{I}$ is the $KLM \times KLM$ identity matrix.

CRB: We compute the Cramér-Rao bound (CRB) [30] to study the estimation accuracy using our approximated forward model (3.18). Here, for estimating the (6×1)–dimensional vector $\boldsymbol{\varphi}$, the $(i, j)^{\mathrm{th}}$ entry $(\forall\, i, j \in \{1, 2, \ldots, 6\})$ of the Fisher information

matrix (see, e.g., [30]) is given by

$$\boldsymbol{J}_{i,j} = \frac{1}{\sigma_{\mathrm{b}}^2} \left[\frac{\partial}{\partial \boldsymbol{\varphi}_i} (\theta \tilde{s}'(x, y, z; \boldsymbol{\eta})) \right]^T \left[\frac{\partial}{\partial \boldsymbol{\varphi}_j} (\theta \tilde{s}'(x, y, z; \boldsymbol{\eta})) \right], \qquad (3.24)$$

where $\boldsymbol{\varphi}_i$ is the ith element ($\forall\ i \in \{1, 2, \ldots, 6\}$) of the parameter vector $\boldsymbol{\varphi}$. We compute the CRB for the unbiased estimates of the parameters in $\boldsymbol{\varphi}$ from the diagonal elements of the matrix $\boldsymbol{J}^{-1}$ [30]. Note that the partial derivatives in (3.24) can easily be computed using the expression of $\theta \tilde{s}'(x, y, z; \boldsymbol{\eta})$, and hence we do not include those details here.

3.4 Numerical Examples

We present two numerical examples comparing the performance of our proposed parameter estimation method with the blind-deconvolution (BD) algorithm [7] and the parametric blind-deconvolution (PBD) algorithm [8]. We also compare the mean-squares errors (MSE) of the estimated parameters in $\boldsymbol{\varphi}$ with their analytical bounds on the variance of error.

3.4.1 Examples: Data Generation

Example 1

In this example, we aim to present the robustness of our proposed algorithm by comparing its performance with the BD and PBD algorithms. We simulate the data here following the ground-truth image distortion phenomenon. Namely, to simulate

the data, we do not follow the object model (3.4), the PSF model (3.6), or the forward model (3.19). We consider the case in which the QDs are randomly placed, and each of their light intensity profiles follows a 3D Gaussian function in space inside each microsphere. We also consider a simple and modified version of the classical PSF model (3.5) proposed in [8], the under-sampling phenomenon encountered while capturing the data in practice, the photon counting process in the CCD, and the additive thermal background noise at the CCD detector output.

We generate the image data for a single-sphere object of radius $r = 1.8\mu$m on a $551 \times 551 \times 551$ voxel sampling lattice with voxel size $\Delta x = \Delta y = \Delta z = 32$nm. We position the QD centers in each voxel location inside the object with a probability of 0.3 [20]. A symmetric 3D Gaussian function with a variance of 64nm produces the light-intensity profile of each QD. We assume here that such light intensity profile is deterministic, and assume a large number to define its maximum value.

We generate the synthetic PSF following the parametric model proposed in [8]. In this model, the exponential phase-term of the classical PSF model (3.5) is replaced with $F(\alpha, z)$, where

$$F(\alpha, z) = D(\alpha) \exp[jW(\alpha, z)] \tag{3.25}$$

is the pupil function of the objective lens. The pupil amplitude function $D(\alpha)$ is given as

$$D(\alpha) = \begin{cases} 1 + a_1\alpha & \text{for} \quad |\alpha| \leq \alpha_0 \\ 0 & \text{otherwise,} \end{cases} \tag{3.26}$$

where a_1 is a known parameter and α_0 is the known cut-off frequency of the objective lens, see [45]. The term $W(\alpha, z)$ is given by

$$W(\alpha, z) = zW_1(\alpha) + W_2(\alpha), \tag{3.27}$$

where $W_1(\alpha)$ and $W_2(\alpha)$ are given as follows:

$$W_1(\alpha) = n_\text{o} \left[1 - \left(\frac{N_\text{a}\alpha}{n_\text{o}} \right)^2 \right]^{1/2} \frac{2\pi}{\lambda}, \tag{3.28}$$

and

$$W_2(\alpha) \approx \sum_{n=0}^{N_\text{b}-1} b_n \alpha^n, \tag{3.29}$$

where $b_0, b_1, b_2, \ldots, b_{N_\text{b}-1}$ are the known parameters of $W_2(\cdot)$, see [45]. We use here $\lambda = 0.63\mu\text{m}$, $N_\text{a} = 1$, $M' = 40$, and $n_\text{o} = 1.515$ to generate the synthetic PSF.

We generate the microscope output by convolving the simulated object image with the PSF generated over the same grid. Image formation is a continuous space process, whereas the estimation takes place on sampled images. To incorporate this difference in our simulation, we sample every fifth voxel intensity along every dimension to obtain a reduced image of $111 \times 111 \times 111$ voxels with $\Delta x = \Delta y = \Delta z = 0.16\mu\text{m}$. Using this image, we generate the photon counts in the CCD as

$$\beta g_\text{c}(x, y, z; \boldsymbol{\varphi}) \sim \mathcal{P}(\beta \tilde{s}(x, y, z; \boldsymbol{\varphi})), \tag{3.30}$$

where $\mathcal{P}(\cdot)$ is a Poisson random variable with mean-rate $\beta \tilde{s}(\cdot)$, and we use $\beta = 10$. We then generate the CCD output by introducing with $g_\text{c}(\cdot)$ the thermal background

57

noise $w_{\mathrm{b}}(\cdot)$ defined in Section 3.2. We vary the variance of this noise using

$$\sigma_{\mathrm{b}}^2 = M_g \sigma_0^2, \tag{3.31}$$

where M_g is the maximum intensity value of $g_{\mathrm{c}}(\cdot)$ at the measured voxels, and σ_0^2 is a user-chosen parameter.

Example 2

In this example, we aim to compare the performance in estimating the unknown parameters with their corresponding CRBs using our proposed algorithm and the BD and PBD algorithms. The data here are simulated using the forward model (3.19).

The image data for a single-sphere object of radius $r = 1.8\mu$m are generated on a $111 \times 111 \times 111$ sampling lattice with voxel size $\Delta x = \Delta y = \Delta z = 0.16\mu$m. We use here $\theta = 10$, and generate the synthetic PSF using (3.6).

To generate the output of the microscope and the CCD detector, we convolve the simulated object image with the microscope PSF generated over the same grid following (3.18).

3.4.2   Parameter Estimation

For both examples, we perform the estimation using the following three methods and compare their performances.

1. *Our proposed algorithm:* We estimate the microsphere center parameters using (3.22). We assume that the object and PSF parameters are unknown.

2. *Parametric blind-deconvolution (PBD) algorithm* (see Appendix C) [8]: We estimate the object as follows:

$$\hat{s}^{(k+1)}(x,y,z) = \frac{\hat{s}^{(k)}(x,y,z)}{H_0} \times \left[h(-x,-y,-z) \otimes \frac{g(x,y,z)}{h(x,y,z) \otimes \hat{s}^{(k)}(x,y,z)} \right],$$
(3.32)

where $s(\cdot), h(\cdot)$, and $g(\cdot)$ denote the object, PSF, and output measurement, respectively; $\hat{s}^{(k)}(\cdot)$ is the estimated object at the kth iteration; and

$$H_0 = \int_z \int_y \int_x h(x,y,z) \mathrm{d}x \mathrm{d}y \mathrm{d}z \ [8].$$
(3.33)

We assume here that the PSF $h(\cdot)$ is known for estimating the object using (3.32). We further define

$$E^{(k+1)} = \sum_z \sum_y \sum_x \left[\hat{s}^{(k+1)}(x,y,z) - \hat{s}^k(x,y,z) \right]^2$$
(3.34)

as the error at the $(k+1)^{\text{th}}$ iteration. We continue iterating (3.32) until

$$\left| \frac{E^{(k+1)} - E^{(k)}}{E^{(k+1)}} \right| < \epsilon,$$
(3.35)

where ϵ is a user-chosen small number.

3. *Conventional blind-deconvolution (BD) algorithm* (see Appendix C) [7]: Here, we simultaneously estimate the unknown PSF and the object using the *deconvblind* command of MATLAB.

Microsphere Location Estimation: Our proposed method in Section 3.3 directly estimates the microsphere center parameters. However, the BD and PBD algorithms do not estimate them quantitatively. Thus, in those cases, we first transform the voxel intensities of the estimated object to zero below a certain threshold level. We then estimate the microsphere centers by averaging the voxel coordinates with nonzero intensity values.

3.4.3   Results and Discussion

We present the estimation performances of the numerical examples in Figures 3.5 and 3.6. Figure 3.5 shows the MSEs of the estimated microsphere center parameter x_c as a function of σ_0^2 for the data in Example 1, where

$$\sigma_0^2[\text{dB}] = \sigma_b^2[\text{dB}] - \frac{1}{2}M_g[\text{dB}]. \tag{3.36}$$

Figure 3.6 shows the MSEs of the estimated microsphere center parameter x_c as a function of the SNR for the data in Example 2. We define the SNR in Example 2 as

$$\text{SNR} = \frac{\left[\max_{x,y,z}\tilde{s}(\cdot) - \min_{x,y,z}\tilde{s}(\cdot)\right]}{\sigma_b}. \tag{3.37}$$

In Example 1 (see Figure 3.5), our algorithm does not perform as well as the BD and PBD algorithms at very low SNR. In Example 2 (see Figure 3.6), PBD outperforms our algorithm at the low SNR, but the estimations using both the PBD and BD fail to achieve the CRB. In the same example, our algorithm performs the best among the three, starting from 5dB, and also achieves the CRB. In summary, in both the
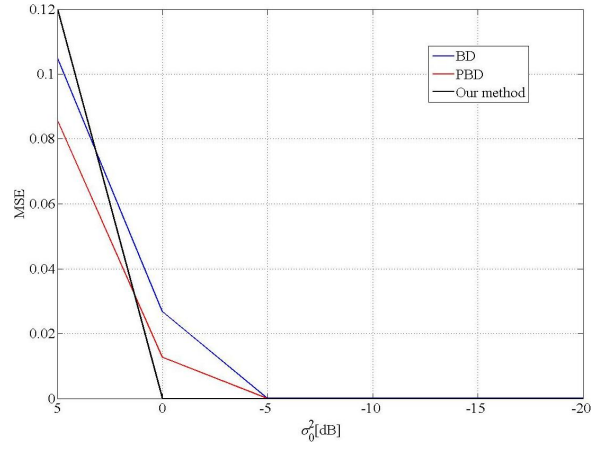
60

Figure 3.5: Mean-square errors of the estimated microsphere center parameter x_c as a function of varying σ_0^2. ©[2008] IEEE.
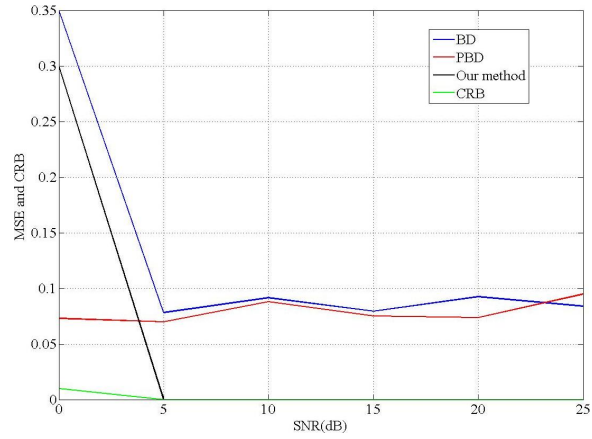
Figure 3.6: Mean-square-errors and Cramér-Rao bound of the estimated microsphere center parameter x_c as a function of signal-to-noise ratio. ©[2008] IEEE.

examples we observe that (i) our algorithm always performs better in the high SNR regions and (ii) BD performs the worst among the three. The main reason for the better performance of our algorithm is that it contains prior information of the object shape (spherical), whereas the other algorithms (BD and PBD) are not based on that assumption. Note that we assume the PSF is known in evaluating the PBD algorithm, since an unknown PSF-based PBD algorithm requires an extensive computational load [8]. Also, the computational speed of BD is the highest among all the three algorithms.

3.5   Estimation Results Using Real Data

This section presents a quantitative estimation analysis of a real-data set using our method and compares the performance with the BD algorithm. The PBD algorithm is not used, as the PSF is unknown for the real data. The PBD algorithm requires a time-intensive computation in estimating the unknown parameters for the case of an unknown PSF. In contrast, the BD algorithm is faster and does not perform in the numerical examples much worse than the PBD algorithm at high SNR (see Figures 3.5 and 3.6). Recall from Section 3.3 that we analyze here microsphere QD light images captured at a high SNR [5], and thus the BD algorithm is sufficient for the performance comparison presented in this section.

3.5.1   Experiment Details

We apply our algorithm and the BD algorithm to a section of microsphere images captured on a $1036 \times 1360 \times 51$ voxel sampling lattice. We extract a section of seven

microsphere images on a $241 \times 340 \times 51$ voxel sampling lattice from this data to test the estimation performance. The radius of the spheres is known as $r = 1.8\mu$m by experimental convention [1], [40]. The imaging is performed using a standard fluorescence microscope with $\lambda = 0.63\mu$m, $N_\mathrm{a} = 1$, $M' = 40$, $n_\mathrm{o} = 1.515$, $n_\mathrm{s} = 1.3$, and $n_\mathrm{g} = 1.5$, and the images are captured using a cooled CCD.

3.5.2 Image Segmentation

We segment single-sphere images of the seven microspheres using the k-means clustering algorithm[7]. We evaluate the k-means algorithm using the *kmeans* command of MATLAB [7]. This evaluation requires prior knowledge of the cluster number, which in our case is equivalent to the number of microspheres in the image. Note that other clustering algorithms can be employed here, such as the mixture of Gaussians [46].

3.5.3 Microsphere Localization and Quantification

From the block of seven microsphere images, we localize and quantify each segmented single-sphere object using our algorithm and the BD algorithm. The BD algorithm does not estimate the unknown parameters x_c, y_c, z_c, and θ quantitatively. Hence, to estimate a microsphere location using BD, we adopt a method similar to that described in Section 3.4.2. To quantify a microsphere intensity using BD, we first average the intensities of the estimated object above a certain threshold level. Then this average intensity is multiplied with the corresponding maximum intensity of the estimated PSF, and the resulting value is used as the estimate of θ.

---

[7]The k-means algorithm is a clustering algorithm to cluster n' objects based on attributes into k' partitions, where $k' < n'$.

3.5.4 Results and Discussion

Figure 3.7 presents our analysis for the real data. The origin is at the center of the seven-microsphere block. Figure 3.7(a) shows the microsphere intensity profile on the focal plane of reference at 0μm. The voxel intensities of the imaged microspheres are set to zero below a certain threshold, and the resultant focal-plane image is shown in Figure 3.7(b). The binary version of this image is shown in Figure 3.7(c), where the nonzero intensities are in red. Figure 3.7(d) presents the segmented version, where different colors specify separated single-sphere objects.

Table 3.1 presents the estimation results of our algorithm and the BD algorithm. This table includes the Euclidean distances between the center location estimates and the intensity level estimates obtained using the two methods. Both algorithms yield similar results for Spheres 1 and 2. This is expected, as we analyze here high-SNR images, and our and BD algorithms perform similarly in the numerical examples for measurements captured at high SNR.

However, we note that the estimation results are slightly different using the two methods for Spheres 3, 5, 6, and 7. These spheres merge into groups of two, and hence their intensities contribute to each other during the convolution operation. Therefore, fitting the single-sphere object model separately to each segmented single-sphere image from a merged image of two spheres does not perform well computationally.

Apart from this, Sphere 4 does not produce a consistent result using either method. In this case, it is not possible to know if the image is produced by the QD light of any microsphere. It might be the case that QDs from a damaged microsphere are illuminated there, because the estimated signal is much weaker.
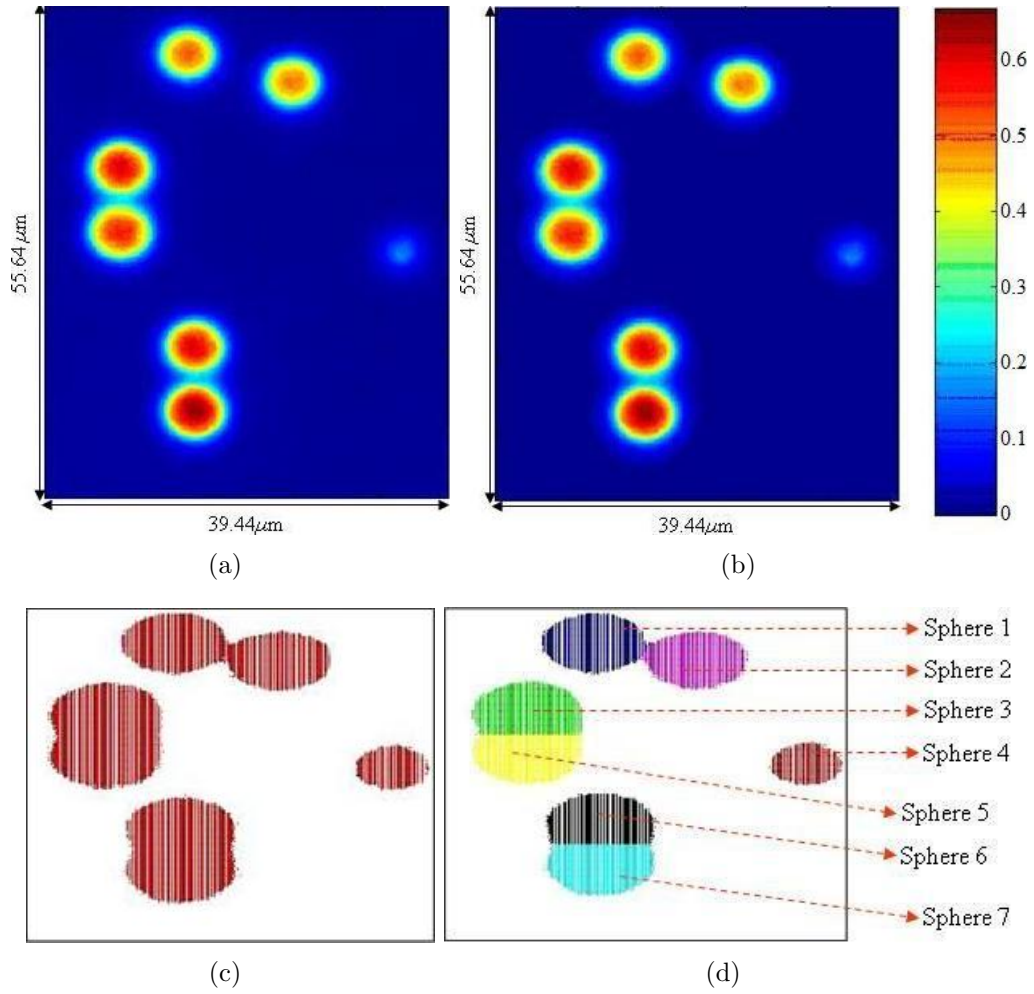
Figure 3.7: Microsphere intensity profile on the focal plane of reference at 0μm of a section of seven microsphere images, (b) their image after a thresholding operation, (c) their binary image, where the red color signifies the nonzero intensities, and (d) their segmented versions, where different colors show separated single-sphere objects. ©[2008] IEEE.

Table 3.1: Comparison of estimation performances using our algorithm and the blind-deconvolution algorithm. ©[2008] IEEE.

	Sphere 1	Sphere 2	Sphere 3	Sphere 4	Sphere 5	Sphere 6	Sphere 7
$\widehat{x}_{\mathrm{c}}(\mu m)$–Our method	-5.78	4.16	-12.5	14.54	-12.45	-5.68	-5.47
$\widehat{x}_{\mathrm{c}}(\mu m)$–BD	-5.78	4.14	-12.30	14.59	-12.27	-5.49	-5.14
$\widehat{y}_{\mathrm{c}}(\mu m)$–Our method	21.89	18.69	9.25	-0.19	2.29	-10.38	-17.38
$\widehat{y}_{\mathrm{c}}(\mu m)$–BD	21.84	18.64	9.33	-0.43	1.97	-10.51	-17.44
$\widehat{z}_{\mathrm{c}}(\mu m)$–Our method	0.02	0.04	-0.04	0.04	0.01	0.07	0.04
$\widehat{z}_{\mathrm{c}}(\mu m)$–BD	0.07	0.05	0.02	0.14	0.14	0.12	0.14
Euclidean distance between the estimated centers (μm)	0.0707	0.0548	0.2236	0.2648	0.3895	0.2356	0.35
$\hat{\theta}(\times 10^{-4})$–Our method	1.1995	1.09	1.41	0.15	1.25	1.26	1.7
$\hat{\theta}(\times 10^{-4})$–BD	1.0237	0.99	1.3	0.06	1.1	1.12	1.53
Euclidean distance between the estimated intensities	0.1758	0.1	0.11	0.09	0.15	0.14	0.17

Chapter 4

Conclusion and Future Work

In this chapter, we first summarize the key contributions of our work in Section 4.1 and then provide future work in Section 4.2.

4.1 Conclusion

In this dissertation, we proposed a three-dimensional microarray with position-encoded microspheres, and discussed its potential advantages. The microarray imaging is performed using a fluorescence microscope and an image sensor.

We developed an optimal statistical design for positioning the microspheres in the microarray. We derived posterior Cramér-Rao bounds on the errors in estimating the target concentrations, for uniform or sparse target profiles. We showed quantitatively the effects of the microsphere distance and operating temperature on the imaging performance. We computed the optimal (minimal) distance between the microspheres at a given temperature using the statistical performance analysis results. The minimal microsphere distance guarantees a desired level of statistical accuracy in imaging the proposed microarray, with efficient microsphere packing. We computed the optimal

operating temperature of the image sensor as a trade off between its cost and the desired statistical performance.

The main advantages of the proposed microarray over existing three-dimensional microarrays are efficient packing, high sensitivity, simplified imaging, and guaranteed accuracy in estimating the target concentrations.

Potential applications include molecular recognition, specificity of targeting molecules, protein-protein dimerization, high throughput screening assays for enzyme inhibitors, drug discovery, gene sequencing, etc.

To compute the optimal design variables, we substituted the maximum likelihood estimates for the true values of the photon-conversion factor of the image sensor and its background noise variance. We estimated these parameters using images of multiple target-free microspheres embedded with quantum-dots and placed randomly on a substrate. We obtained the photon-conversion factor using a method-of-moments estimation, where we replaced the quantum-dot intensity levels and locations of the imaged microspheres with their maximum likelihood estimates.

We finally developed a maximum likelihood method to estimate the intensity levels and locations of quantum-dot embedded microspheres from their image. The proposed estimation is motivated by the fact that in fluorescence microscopy imaging when the object shape is simple, it can be easily modeled using simple parametric forms with the unknown information of interest as parameters. Then, a problem-specific estimation algorithm can be developed using a maximum likelihood method. This avoids the need of using a commercial deconvolution software, which is often

costly and time intensive to run. We demonstrated that our algorithm achieves robust performance in estimation and outperforms the existing blind-deconvolution algorithms at practical high signal-to-noise ratio scenarios for quantum-dot light imaging. We also found that our and existing blind-deconvolution algorithms perform similarly for real-data images of well-separated microspheres.

Our collaborators are currently implementing the position-encoded three-dimensional microarray device using the minimal separation distance between the microspheres.

4.2   Future Work

In our future work, we will derive tighter bounds to analyze the statistical performance of imaging our proposed microarrays at a low signal-to-noise ratio, fitting the sparse-shell models. We will also model the effect of the actual device on the nanosphere lights, and modify our object models in (2.5) and (2.7) accordingly.

In our implementation, we will maximize the exposed surface area of the microspheres for capturing targets. This is because the device might restrict the microsphere surface area that can interact with targets. We will also maximize the microsphere packing in the proposed device. Our optimization analysis will consider the estimation errors associated with the specific device structure. We will further compute the number of nanospheres required to detect a single target using our device.

We will develop algorithms to estimate the target concentrations in the device, for sparse target profiles. For uniform target profiles, the concentration estimation algorithm will essentially be similar to what we developed in Chapter 3. Here the only

difference will be that we will need to use the full-shell model (2.5) as the unknown object model.

We will also conduct experiments to simultaneously screen complementary DNA, RNA, and protein receptors to exemplify the potential advantages of the device. Assuming that the bindings are specific, we will demonstrate the ability, through efficient processing, to identify targets on a single platform without errors. The position encoding and use of an identical detection strategy for different target types should simplify screening and avoid errors in target quantification and identification. One of the potential experiments will be investigating tumor proliferation in screening different patients.

In long term research, we aim to analyze the performance of our device through computing its specificity and sensitivity, incorporating experimental measurements of non-specific bindings.

Appendix A

Monte-Carlo Integration Estimation

We present the Monte-Carlo integration estimation technique [28] for single parameter cases, which can be easily extended for multi-parameter cases. Suppose we wish to compute integrals of the form

$$V = \int v(\omega) p_\Omega(\omega) \mathrm{d}\omega, \tag{A.1}$$

where $v(\omega)$ is a function of the variable ω and $p_\Omega(\omega)$ is a pdf. We generate a large N' number of samples $\vartheta_{n'}$ of ω from $p_\Omega(\omega)$ and compute the Monte-Carlo estimate of the integral (A.1):

$$\widehat{V} = \frac{1}{N'} \sum_{n'=1}^{N'} v(\vartheta_{n'}). \tag{A.2}$$

The accuracy of $\widehat{V}$ depends on N', but is independent of $\dim(\omega)$ (i.e., the dimensionality of the integral (A.1)). By the law of large numbers,

$$\lim_{N'\to\infty} \widehat{V} = V. \tag{A.3}$$

Appendix B

Proof of Equation (2.36)

For each microsphere image segment, we have from (2.34),

$$
\begin{aligned}
\frac{\tilde{s}(x,y,z;\boldsymbol{\gamma})}{\beta} + \sigma_{\mathrm{b}}^2 &= \mathrm{E}[(g(x,y,z;\boldsymbol{\gamma}) - \tilde{s}(x,y,z;\boldsymbol{\gamma}))^2] \qquad (\mathrm{B.1}) \\
&\approx (g(x,y,z;\boldsymbol{\gamma}) - \tilde{s}(x,y,z;\boldsymbol{\gamma}))^2.
\end{aligned}
$$

In (B.1), replacing $\boldsymbol{\gamma}$ by its corresponding estimate $\hat{\boldsymbol{\gamma}}$ and averaging both sides over all the voxels of the microsphere image segment of interest, we obtain (2.36).

Appendix C

Blind Deconvolution[8]

In this appendix, we review the Richardson-Lucy (RL) algorithm [11]. We then discuss the blind-deconvolution (BD) algorithm embedded in MATLAB and the parametric blind-deconvolution (PBD) algorithm.

The RL algorithm was originally developed from Bayes's theorem. This theorem is given by

$$P(u|v) = \frac{P(v|u)P(u)}{\int P(v|u)P(u)\mathrm{d}u}, \tag{C.1}$$

where $P(v|u)$ is the conditional probability of the event v given u, $P(u)$ is the probability of the event u, and $P(u|v)$ is the inverse conditional probability, i.e., the probability of event u given event v. The probability $P(u)$ can be identified as the object distribution $s(u)$; the conditional probability $P(v|u)$ can be identified as the point-spread function (PSF) centered at u, i.e., $h(v, u)$; and the probability $P(v)$ can be identified as the degraded image $g(v)$. The inverse relation of the iterative

---

[8]Based on "Estimating locations of quantum-dot–encoded microparticles from ultra-high density 3D microarrays," by P. Sarder and A. Nehorai, in *IEEE Trans. on NanoBioscience,* vol. 7, pp. 284-297, Dec. 2008. ©[2008] IEEE.

algorithm is given by

$$s_{i+1}(u) = \int \frac{h(v,u)g(v)\mathrm{d}v}{\int h(v,w)s_i(w)\mathrm{d}w} s_i(u), \tag{C.2}$$

where i is the iteration number. Under an isoplanatic condition, we write (C.2) as

$$s_{i+1}(x) = \left\{ \left[\frac{g(x)}{s_i(x) \otimes h(x)} \right] \otimes h(-x) \right\} s_i(x), \tag{C.3}$$

where $\otimes$ denotes the convolution operation [41].

For a known PSF $h(x)$, we estimate $s(x)$ by iterating (C.3) until convergence. To start the algorithm, we require here an initial guess $s_0(x)$. If $s_0(x) \geq 0$, this algorithm assures a positive $s(x)$. It also conserves the energy in the iterations.

The blind form of the RL algorithm is given by

$$h_{i+1}^{(k)}(x) = \left\{ \left[\frac{g(x)}{h_i^{(k)}(x) \otimes s^{(k-1)}(x)} \right] \otimes s^{(k-1)}(-x) \right\} h_i^{(k)}(x), \tag{C.4}$$

$$s_{i+1}^{(k)}(x) = \left\{ \left[\frac{g(x)}{s_i^{(k)}(x) \otimes h^{(k)}(x)} \right] \otimes h^{(k)}(-x) \right\} s_i^{(k)}(x). \tag{C.5}$$

We compute (C.4) and (C.5) at the kth blind iteration of this algorithm using the estimated object from the $(k-1)^{\text{th}}$ blind step. The loop is repeated until convergence. Start the algorithm requires initial guesses $s_0^0(x)$ and $h_0^0(x)$. If $s_0^0(x) \geq 0$ and $h_0^0(x) \geq 0$, this algorithm assures positive $s(x)$ and $h(x)$.

The BD algorithm embedded in MATLAB uses an accelerated and damped version of the RL algorithm specified by (C.4) and (C.5) [7].

The PBD algorithm was derived in [8] assuming that the measurement $g(x)$ is $(s(x) \otimes h(x))$ corrupted by a Poisson noise [20]. The authors in [8] also proposed a parametric PSF model that we review in Section 3.4.1. They then used an expectation maximization formulation [30] to maximize the likelihood. In the resulting algorithm, the object is updated using a similar iterative form as (C.3); see also (3.32). The parameters of the PSF are updated using a numerical method at each PBD step; see [8] for more details. In our numerical example in Section 3.4.1, we assume that the PSF is known in (3.32) for simplicity.

References

[1] A. Mathur, *Image Analysis of Ultra-High Density, Multiplexed, Microsphere-Based Assays,* Ph.D. thesis, Northwestern University, IL., 2006.

[2] P. Sarder, A. Nehorai, P. H. Davis, and S. Stanley, "Estimating gene signals from noisy microarray images," *IEEE Trans. on NanoBioscience,* vol. 7, pp. 142-153, 2008.

[3] W. Xu, K. Sur, H. Zeng, A. Feinerman, D. Kelso, and J. B. Ketterson, "A microfluidic approach to assembling ordered microsphere arrays," *J. of Micromechanics and Microengineering,* vol. 18, p. 075027, 2008.

[4] K. D. Bake and D. R. Walt, "Multiplexed spectroscopic detections," *Annu. Rev. Anal. Chem.,* vol. 1, pp. 15-47, 2008.

[5] M. Han, X. Gao, J. Z. Su, and S. Nie, "Quantum-dot-tagged microbeads for multiplexed optical coding of biomolecules," *Nat. Biotechnol.,* vol. 19, pp. 631-635, 2001.

[6] Crystalplex Corporation, Pittsburgh, PA: *http://www.crystalplex.com.*

[7] MATLAB software package, The MathWorks: *http://www.mathworks.com/products/matlab/.*

[8] J. Markham and J. Conchello, "Parametric blind deconvolution: A robust method for the simultaneous estimation of image and blur," *J. Opt. Soc. Am. A,* vol. 16, pp. 2377-2391, 1999.

[9] S. F. Gibson and F. Lanni, "Experimental test of an analytical model of aberration in an oil-immersion objective lens used in three-dimensional light microscopy," *J. Opt. Soc. Am. A,* vol. 8, pp. 1601-1612, 1991.

[10] H. L. van Trees, *Detection, Estimation and Modulation Theory,* New York: Wiley, 1968.

[11] P. Sarder and A. Nehorai, "Deconvolution methods of 3D fluorescence microscopy images: An overview," *IEEE Signal Proc. Magazine,* vol. 23, pp. 32-45, 2006.

[12] M. Christenson, "The application of scientific grade CCD cameras to biological imaging," *Imaging Neurons: A Laboratory Manual,* Ch. 6, R. Yuste, F. Lanni, A. Konnerth, Eds., pp. 23-32, 2000.

[13] *http://www.wateccameras.com/index.php.*

[14] *http://www.sac-imaging-europe.com/PDF Files/Micron_MT9M_Product_sheet.pdf.*

[15] P. Sarder and A. Nehorai, "Estimating locations of quantum-dot–encoded microparticles from ultra-high density 3D microarrays," *IEEE Trans. on NanoBioscience,* vol. 7, pp. 284-297, 2008.

[16] D. L. Snyder and M. I. Miller, *Random Point Processes in Time and Space, 2nd Ed.,* New York: Springer-Verlag, 1991.

[17] T. M. Jovin and D. J. Arndt-Jovin, "Luminescence digital imaging microscopy," *Annu. Rev. of Biophysics and Biophysical Chem.,* vol. 18, pp. 271-308, 1989.

[18] G. M. P. van Kempen, *Image Restoration in Fluorescence Microscopy,* Ph. D. thesis, Delft Technical University, Delft, The Netherlands, 1999.

[19] J. Ohta, *Smart CMOS Image Sensors and Applications,* CRC Press, 2007.

[20] A. Papoulis and S. U. Pillai, *Probability, Random Variables and Stochastic Processes, 4th Ed.,* McGraw-Hill Science, 2001.

[21] E. I. George and D. P. Foster, "Calibration and empirical Bayes variable selection," *Biometrika,* vol. 87, pp. 731747, 2000.

[22] E. G. Larsson and Y. Selén, "Linear regression with a sparse parameter vector," *IEEE Trans. on Signal Proc.,* vol. 55, pp. 451-460, 2007.

[23] S. Ji, Y. Xue, and L. Carin, "Bayesian compressive sensing," *IEEE Trans. Signal Proc.,* vol. 56, pp. 2346-2356, 2008.

[24] J. G. McNally, T. Karpova, J. Cooper, and J. A. Conchello, "Three-dimensional imaging by deconvolution microscopy," *Methods,* vol. 19, pp. 373-385, 1999.

[25] P. J. Verveer, *Computational and Optical Methods for Improving Resolution and Signal Quality in Fluorescence Microscopy,* Ph. D. thesis, Delft Technical University, Delft, The Netherlands, 1998.

[26] H. T. M. van der Voort and K. C. Strasters, "Restoration of confocal images for quantitative image analysis," *J. of Microscopy,* vol. 178, pp. 165-181, 1995.

[27] P. Tichavsky, C. H. Muravchik, and A. Nehorai, "Posterior Cramér-Rao bounds for discrete-time nonlinear filtering," *IEEE Trans. on Signal Proc.,* vol. SP-46, pp. 1386-1396, 1998.

[28] G. Casella, *Monte Carlo Statistical Methods, 2nd Ed.,* Springer Verlag, 2004.

[29] Y. S. Chow and H. Teicher, *Probability Theory: Independence, Interchangeability, Martingales, 3rd Ed.,* Springer, 2003.

[30] S. M. Kay, *Fundamentals of Statistical Signal Processing, Estimation Theory,* Englewood Cliffs, NJ: PTR Prentice Hall, 1993.

[31] F. Pukelsheim, "Information increasing orderings in experimental design theory," *Int. Stats. Rev.,* vol. 55, pp. 203-219, 1987.

[32] F. Pukelsheim, *Optimal Design of Experiments, 1st Ed.,* John Wiley & Sons, Inc., 1993.

[33] K. Shah and B. Sinha, *Theory of Optimal designs,* New York: Springer-Verlag, 1989.

[34] B. V. V. Zeghbroeck, *Principles of Semiconductor Devices and Heterojunctions,* Prentice Hall, 2008.

[35] R. V. Hogg and A. T. Craig, *Introduction to Mathematical Statistics, 5th Ed.,* Prentice Hall, 1995.

[36] B. Porat, *Digital Processing of Random Signals: Theory and Methods,* Englewood Cliffs, NJ: Prentice Hall, 1994.

[37] G. Strang, *Introduction to Linear Algebra, 3rd Ed.,* Wellesley-Cambridge Press, 2003.

[38] *http://www.zeiss.com/C1256D18002CC306/0/974174FE5C0B97FBC1256D590 0335191/$file/40-083$_e$.pdf.*

[39] *http://www.smt.zeiss.com/0625690B000338EF/Contents-Frame/4AE544FB791F7753C1256BF80043CCB2.*

[40] A. Mathur and D. M. Kelso, "Segmentation of microspheres in ultra-high density microsphere-based assays," *Proceed. of SPIE,* vol. 6064, pp. 60640B1-60640B10, 2006.

[41] A. V. Oppenheim, A. S. Willsky, S. Hamid, and S. H. Nawab, *Signals and Systems, 2nd Ed.,* Prentice Hall, 1996.

[42] T. J. Holmes, "Maximum-likelihood image restoration adapted for non coherent optical imaging," *J. Opt. Soc. Am. A,* vol. 5, pp. 666-673, 1988.

[43] B. Zhang, J. Zerubia, and J. O. Martin, "Gaussian approximations of fluorescence microscope point spread function models," *Applied Optics,* vol. 46, pp. 1819-1829, 2007.

78

[44] D. Kundur and D. Hatzinakos, "Blind image deconvolution," *IEEE Signal Proc. Magazine,* vol. 13, pp. 43-64, 1996.

[45] J. A. Conchello and Q. Yu, "Parametric blind deconvolution of fluorescence microscopy images: Preliminary results," in *Three-Dimensional Microscopy: Image Acquisition and Processing III,* C. J. Cogswell, G. Kino, and T. Willson, Eds. *Proceed. of SPIE,* vol. 2655, pp. 164-174, 1996.

[46] T. Hastie, R. Tibshirani, J. H. Friedman, *The Elements of Statistical Learning,* Springer, 2003.

Vita

Pinaki Sarder (psarde1@ese.wustl.edu)

6060 Pershing Av., Apt# 202, St. Louis, MO 63112, Ph# 314-935-4146 (O)

Summary: Doctoral Candidate in Electrical and Systems Engineering Department at Washington University in St. Louis, graduating in Spring 2010. Ph.D. work involves Designing and Imaging of Position-Encoded 3D Microarrays and Genomic Signal Processing under the guidance of Dr. Arye Nehorai, who is an eminent researcher in the field of Sensor Array Signal Processing. Co-authorships with researchers from Washington University School of Medicine, including the former Vice Chancellor for Research, Dr. Samuel L. Stanley. Recipient of an Imaging Sciences Pathway Fellowship from the Division of Biology and Biomedical Sciences at Washington University School of Medicine in 2007. B.Tech. in Electrical Engineering from the Indian Institute of Technology, Kanpur, India.

Research Interests: Statistical Signal Processing, Medical Imaging, Optimal Design of Experiments, and Genomic Signal Processing.

Research Skills:

- Applying techniques from Detection and Estimation theory, including Maximum Likelihood Estimation, Bayesian Estimation, Markov Chain Monte Carlo Sampling (e.g., Gibbs Sampling, Jump Diffusion), Cramér-Rao Bound (classical and posterior), Generalized Likelihood Ratio Test.

- Statistical Modeling and Analysis using techniques from Linear Statistical Inference theory and Multivariate theory.

- Physical Modeling.

Education:

- *2003 to present:* Ph.D. Candidate in Electrical and Systems Engineering at Washington University in St. Louis; Adviser: Prof. Arye Nehorai; Dissertation: *Statistical Design and Imaging of Position-Encoded 3D Microarrays*; GPA: 4/4.

- *2010:* M.Sc. in Electrical Engineering will be granted at Washington University in St. Louis; Adviser: Prof. Arye Nehorai; GPA: 4/4.

- *1999 to 2003:* B.Tech. in Electrical Engineering at the Indian Institute of Technology, Kanpur, India; GPA: 8.5/10.

Research Experience:

- *Jan 2006 to present:* Research Assistant in the Center for Sensor Signal and Information Processing of the Electrical and Systems Engineering Department at Washington University in St. Louis; Adviser: Prof. Arye Nehorai; Research in Microarray Imaging and Genomics; Hands-on experience in Photolithography.

- *Jan 2007 to Dec 2007:* Research Trainee in the Imaging Sciences Pathway program of the Division of Biology and Biomedical Sciences at the Washington University School of Medicine.

- *May 2004 to Dec 2005:* Research Assistant in the Signal and Image Research Laboratory of the Electrical and Computer Engineering Department at the University of Illinois at Chicago; Adviser: Prof. Arye Nehorai; Research in Microarray Imaging.

Award:

- Recipient, Imaging Sciences Pathway program Graduate Student Fellowship, Washington University School of Medicine, January 2007 to December 2007.

Activities:

- Reviewer: *IEEE Trans. on Medical Imaging*; *IEEE Trans. on NanoBioscience*; *IEEE Signal Processing Letters*; *Image and Vision Computing, Elsevier.*

- Student Member: Imaging Sciences Pathway program steering committee, Division of Biology and Biomedical Sciences at Washington University School of Medicine, January 2008 to December 2008.

- Host: Imaging Sciences Pathway student-sponsored seminar (invited Dr. J. Kovačević, Professor of Biomedical Engineering and Electrical and Computer

Engineering, Carnegie-Mellon University, to present a talk in Electrical and Systems Engineering and Division of Biology and Biomedical Sciences, Washington University in St. Louis, on *Problems in Biological Imaging: Opportunities for Signal Processing*, Mar. 7, 2008).

Thesis:

- P. Sarder, *Statistical Design and Imaging of Position-Encoded 3D Microarrays,* Ph.D. thesis, Washington University in St. Louis, MO, USA, in preparation.

Book Chapter:

1. **P. Sarder**, W. Zhang, J. P. Cobb, and A. Nehorai, "Gene reachability using Page ranking on gene co-expression networks," in revision for *Link Mining: Models, Algorithms, and Applications,* Ch. 11, P. S. Yu, C. Faloutsos, and J. Han, Eds., Springer.

Journal Papers:

1. **P. Sarder** and A. Nehorai, "Deconvolution methods for 3D fluorescence microscopy images: An overview," *IEEE Signal Processing Magazine,* vol. 23, no. 3, pp. 32–45, May 2006. [This paper has received 25 citations according to the ISI citation index and 48 citations according to Google Scholar, Feb. 6, 2010. "Sarder and Nehorai review perhaps the most heavily studied signal processing topic related to fluorescence microscopy: the deconvolution of images to remove blurring inherent in microscope image acquisition." —J. Kovačević and R. F. Murphy (commented in their article, "Molecular and cellular bioimaging," *IEEE Signal Processing Magazine,* vol. 23, no. 3, pp. 19, May 2006).]

2. **P. Sarder,** A. Nehorai, P. H. Davis, and S. Stanley, "Estimating gene signals from noisy microarray images," *IEEE Trans. on NanoBioscience,* vol. 7, no. 2, pp. 142–153, June 2008 (received 1 citation according to the ISI citation index and Google Scholar, Dec. 19, 2009).

3. **P. Sarder** and A. Nehorai, "Estimating locations of quantum-dot–encoded microparticles from ultra-high density 3D microarrays," *IEEE Trans. on NanoBioscience,* vol. 7, no. 4, pp. 284–297, Dec. 2008.

4. **P. Sarder,** W. Schierding, J. P. Cobb, and A. Nehorai, "Estimating sparse gene regulatory networks using a Bayesian linear regression," to appear in *IEEE Trans. on NanoBioscience.*

5. **P. Sarder** and A. Nehorai, "Statistical design of position-encoded 3D microarrays," submitted to *IEEE Sensors Journal.*

Conference Papers:

1. **P. Sarder** and A. Nehorai, "Performance analysis of quantifying fluorescence of target-captured microparticles from microscopy images," *Proc. Fourth IEEE Workshop on Sensor Array and Multi-channel Processing,* pp. 289–293, Waltham, Massachusetts, USA, Jul. 2006.

2. **P. Sarder** and A. Nehorai, "Statistical design of a 3D microarray with position-encoded microspheres," *Proc. Third International Workshop on Computational Advances in Multi-Sensor Adaptive Processing (CAMSAP),* pp. 161–164, Aruba, Dutch Antilles, Dec. 2009.

Talks & Posters:

1. "Statistical design of position-encoded 3D microarrays," invited talk in *Biostatistics, Harvard School of Public Health, Boston, Massachusetts, USA,* Jan. 15, 2010.

2. "Statistical design and imaging of an ultra-high density 3D microarray," invited talk in *Electrical Engineering, Indian Institute of Technology, Bombay, India,* Nov. 20, 2009.

3. "Statistical design and imaging of an ultra-high density 3D microarray," talk in *Electrical and Systems Engineering, Washington University in St. Louis,* Jan. 16, 2009.

4. "Complementary DNA microarray image segmentation," poster in *Imaging Sciences Retreat, Division of Biology and Biomedical Sciences, Washington University School of Medicine,* Apr. 18, 2008.

5. "Gene ranking using the Page-Rank algorithm," talk in *Systems Analysis Group, Washington University in St. Louis,* Sep. 5, 2007.

6. "Locating quantum-dot encoded microparticles from ultra-high-density 3D microarrays," talk in *Imaging Sciences Symposium, Division of Biology and Biomedical Sciences, Washington University School of Medicine,* Jul. 18, 2007.

Course Work: Detection and Estimation Theory, Linear Statistical Inference, Multivariate Analysis, Adaptive Filter Theory, Random Signal Analysis, Advanced Statistical Theory, Advanced Stochastic Models, Advanced Digital Signal Processing, Advanced Digital Communication, Linear Systems, Linear and Nonlinear Programming, Game Theory, Nonparametric Statistics.

Teaching Experience:

- *May 2007 to Dec 2009:* Instructor of study groups on Detection and Estimation Theory, Introduction to Mathematical Statistics, Linear Statistical Models, Multivariate Analysis, and Matrices; Responsible for teaching as well as assigning, grading, and correcting homework for junior graduate students; Responsible for preparing lecture notes on Introduction to Mathematical Statistics, Linear Statistical Models, and Multivariate Analysis.

- *Aug 2003 to Apr 2004:* Teaching Assistant for Electronic Circuit course (ECE340) in the Electrical and Computer Engineering Department at the University of Illinois at Chicago; Responsible for teaching, supervising laboratory experiments, grading and correcting exams and homework assignments for undergraduate students.

Other Skills & Professional Affiliations:

- Programming: C, MATLAB.

- Student Member: IEEE Signal Processing Society, IEEE Communication Society, IEEE Engineering in Medicine and Biology Society.

May 2010

Microarray Design and Imaging, Sarder, Ph.D., 2010